Schweizerische Eidgenossenschaft
Confédération suisse
Confederazione Svizzera
Confederaziun svizra

Federal Department of the Environment, Transport, Energy and Communications DETEC

Swiss Federal Office of Energy SFOE
Energy Research and Cleantech

SWEET Call 1-2020: SWEET EDGE

Deliverable report

Deliverable n°	D6.7 10.2025-1.2026 EPFL-C
Deliverable name	Demonstration Project Alpine-PV: Muttsee (GL) Performance analysis and snow induced losses
Authors The authors bear the entire responsibility for the content of this report and for the conclusions drawn therefrom.	Yael Frischholz, EPFL, **yael.frischholz@epfl.ch** Jérôme Dujardin, Sunwell Sàrl Annelen Kahl, Sunwell Sàrl Michael Lehning, EPFL, **michael.lehning@epfl.ch**
Delivery date	February 2026

sweet swiss energy research for the energy transition

Contents

1 Introduction **1**

2 Site Description **3**
2.1 Location . . . 3
2.2 Power Plant Layout . . . 3
2.3 Monitoring Infrastructure . . . 4
2.3.1 Power variables . . . 4
2.3.2 Environmental variables . . . 5
2.3.3 Camera system . . . 5
2.3.4 Drone surveys . . . 6
2.4 Data Availability . . . 7
2.4.1 Operational timeline and analysis period . . . 7
2.4.2 Monitoring System Uptime . . . 8
2.4.3 Camera Time Series . . . 9
2.5 Data Preprocessing . . . 11
2.6 Meteorological Conditions . . . 11
2.6.1 Solar Irradiance . . . 11
2.6.2 Snow Cover . . . 12
2.6.3 Air Temperature . . . 13
2.6.4 Wind Speed . . . 13

3 Performance Analysis **15**
3.1 Key Performance Indicators . . . 15
3.2 Results . . . 15

4 Snow-Induced Losses **20**
4.1 Method . . . 20
4.1.1 Snow Event and Interference Detection . . . 21
4.1.2 Interference-Induced Losses . . . 22
4.1.3 Correction for Outages in 2024 . . . 22
4.2 Results . . . 23

5 Modeling Interference Height **26**
5.1 Background . . . 26
5.2 Model Development . . . 27
5.2.1 Model Parameters . . . 27
5.2.2 Principal Component Analysis . . . 28
5.2.3 Linear Model . . . 29
5.3 Results . . . 29

6 Conclusion, Limitations, and Outlook **32**

References **34**

A Technical Specifications I

B Drone Surveys V

C Plant Outage 2024: Detailed Table-Level Evolution Maps VI

D Snow Event Catalogue IX

E Principal Component Analysis XII

Summary

This report presents an analysis of the first four years of operation (2022–2025) of the Muttsee photovoltaic power plant, Switzerland's first utility-scale Alpine-PV installation. Located at 2476 m of elevation on the Muttsee dam in Glarus, the plant was commissioned in September 2022 with an installed capacity of 2184 kWp. Monitoring data from SCADA systems, a dedicated camera system, and annual drone surveys enable detailed performance and snow loss analysis.

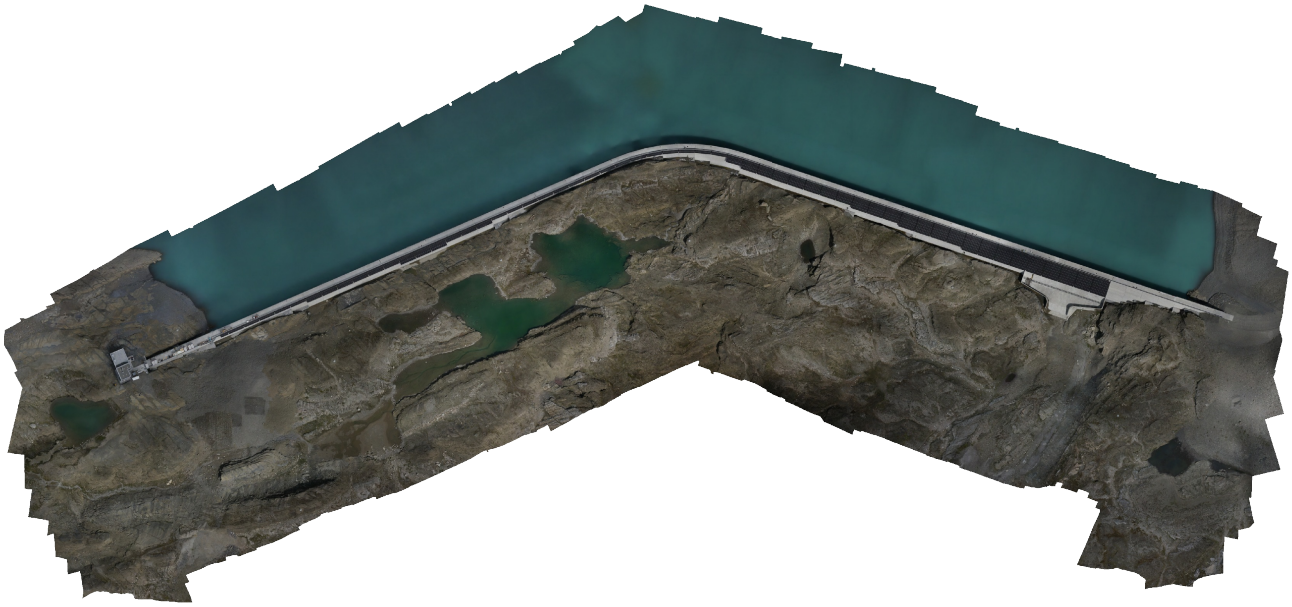
Key findings:

- **Alpine-PV performance confirmed at scale.** Mean annual final yield reached 1211 kWh/kWp ($CF \approx 13.8\%$), with a winter production share approaching 50%. Excluding the 2023/24 season, anomalous for its extreme snow precipitations, yield rises to 1303 kWh/kWp ($CF \approx 14.9\%$).
- **Significant advantage over lowland PV.** Muttsee produced 14.1% more annually than a comparable midland plant, with a winter share increased by 72%. During the months of December to February, this advantage is most pronounced: excluding 2023/24, Muttsee yielded 3.3 times (330%) more than the Payerne midland plant on average (288 vs 87 kWh/kWp). The Solar Express subsidy threshold of 500 kWh/kWp winter production was achieved in two of three winters.
- **Size effects reduce yields compared to test sites.** Compared to the Totalp test site at similar tilt, Muttsee yielded 21.6% less annually and 26.7% less in winter. Effects of the utility-scale power plant size such as heterogeneous orientations, snow-induced losses, and partial outages can explain the difference.
- **Snow losses are limited under normal conditions.** Excluding 2023/24, mean annual snow losses were 40.7 MWh (2.6% of theoretical production), with snow burying contributing 22% of losses.
- **Sub-module clearance height is critical.** The 2023/24 season experienced exceptional snowfall leading to prolonged module burial. Snow losses reached 139.3 MWh (13.3% of theoretical production), rising to 245.5 MWh when including outage-induced losses. Loss due to snow burial accounted for 67% of total losses that season.
- **Structural damage from extreme snow.** The 2023/24 winter caused damage requiring plant shutdown and permanent removal of approximately 9% of installed capacity.
- **Empirical model for interference height.** A linear model based on local snow climatology, topography-corrected dissipation ratio, and projected panel slant length explains 89% of variance in snow accumulation beneath modules ($R^2 = 0.89$, RMSE = 0.58 m) when excluding the anomalous 2022 survey. Residual bias suggests wind-transported snow contributes to accumulation beyond gravitational shedding alone.

Main conclusion: The Muttsee power plant delivered winter electricity as expected with limited snow-related losses. In comparison to ideal test-sites, yields were lower at Muttsee. If snow accumulating beneath the modules reaches their bottom edge, interfering with the shedding process, snow losses and the risk of damage increase rapidly, underscoring the importance of adequate design margins for extreme snow years. The proposed empirical model provides a first tool for estimating required clearance heights, though further refinement incorporating wind-transported snow dynamics is needed.

DEMONSTRATION PROJECT ALPINE-PV: MUTTSEE (GL)

PERFORMANCE ANALYSIS AND SNOW INDUCED LOSSES



AUTHORS:

Yael Frischholz
Laboratory of Cryospheric Sciences (CRYOS)
Ecole Polytechnique Fédérale de Lausanne (EPFL)
Lausanne, Switzerland
CRediT: Writing, Software, Methodology, Analysis, Conceptualization.
Contact: yael.frischholz@epfl.ch

Jérôme Dujardin
Sunwell Sàrl
Lausanne, Switzerland
CRediT: Software

Annelen Kahl
Sunwell Sàrl
Lausanne, Switzerland
CRediT: Funding

Michael Lehning
Laboratory of Cryospheric Sciences (CRYOS)
Ecole Polytechnique Fédérale de Lausanne (EPFL)
Lausanne, Switzerland
CRediT: Review, Funding, Supervision, Conceptualization

ACKNOWLEDGEMENTS:

SWEET-EDGE
The research published in this publication was carried out with the support of the Swiss Federal Office of Energy SFOE as part of the SWEET consortium EDGE. The authors bear sole responsibility for the conclusions and the results presented in this publication.

Innosuisse
This work was partly supported by Innosuisse. Project ID: 47985.1 IP-EE



Muttsee, Curve and East sectors, 18.04.2023

1 Introduction

The photovoltaic (PV) power plant of Muttsee is located on the reservoir dam of the Muttsee in Glarus, Switzerland, at almost 2500 meters of elevation. Due to its size, remote location, and expected high winter electricity production, it is known as the first Swiss, utility-scale, Alpine-PV power plant. It was officially and entirely connected to the grid in September 2022.

From a climatological perspective, high Alpine regions above the fog layer receive significantly more sunshine during the winter months than the Swiss lowlands. This contrast arises from the frequent occurrence of fog and low stratus clouds that blanket the Swiss Plateau, particularly between autumn and winter, while Alpine summits enjoy clear skies and intense solar radiation (Scherrer and Appenzeller, 2014).
The potential of Alpine environments for PV electricity generation has been recognized for decades. Pioneering research at the Jungfraujoch (3454 m a.s.l.) provided ten years of operational data from 1994 to 2003, demonstrating a capacity factor of approximately 16%, a mean annual final yield of 1398 kWh/kWp, and a remarkable winter share of 46.2% (Haeberlin, 2004). These figures contrast with the average yield of Swiss PV systems in the lowlands, estimated at around 954 ± 36 kWh/kWp (Hostettler, 2022) in 2022.
Historically, PV systems in mountain areas were primarily deployed for off-grid applications in remote locations not connected to the electricity network, such as mountain huts, telecommunications infrastructure, and monitoring stations. However, research has highlighted several synergistic advantages of steeply tilted, high-elevation PV installations: low winter sun angles become favorable for energy capture, steep tilts facilitate snow shedding from panel surfaces, and the reflected component of plane-of-array irradiance increases substantially in high-albedo snow-covered environments (Kahl et al., 2019; von Rütte et al., 2021).
With Switzerland's Energy Strategy 2050, initiated in 2011 and enacted into law in 2018, came renewed interest in diversifying domestic renewable electricity production. Political momentum accelerated significantly in 2022 amid geopolitical instability, which heightened concerns over energy security and dependence on foreign electricity imports. In response, the Swiss Parliament passed urgent legislation known as the "Solar Express" in autumn 2022, establishing simplified approval processes and substantial federal subsidies (up to 60% of investment costs) for large-scale alpine solar plants capable of producing significant electricity during winter months. While ambitious, these Alpine-PV projects still face considerable technical challenges, including snow-related impacts on system performance and the verification of real electricity yields, the latter being a critical criterion for the subsidy mechanisms embedded in the new legal framework.
In this context, the pioneering installation at Muttsee was integrated into the Swiss Energy research for the Energy Transition (SWEET) program as demonstration project within the EDGE consortium. The purpose of this federal-level program, launched in 2021 by the Swiss Federal Office of Energy (SFOE), is to accelerate innovations that are key to implementing Switzerland's Energy Strategy 2050 and achieving the country's climate goals. Within SWEET-EDGE, the Muttsee power plant serves as a real-world experiment for Alpine-PV technology, providing empirical data on system performance, snow-related losses, and the scalability of test-scale findings to utility-scale installations. The Swiss innovation agency, Innosuisse also supported this work (Grant: 47985.1 IP-EE).

Since 2022, a comprehensive monitoring system has been deployed at the site. Power output measurements are recorded at the table, string-box, and inverter levels, enabling detailed performance analysis across the plant's hierarchy. Environmental monitoring includes module temperature sensors and plane-of-array irradiance sensors. Additionally, a camera system scans the power plant every five minutes, providing

high-resolution panoramic imagery throughout the winter seasons. Annual drone flights complement these observations by mapping snow height distribution and computing snow accumulation beneath the PV modules.

This report provides an overview of the first four years of the power plant's operations, from 2022 through 2025. It aims to evaluate the electricity generation performance with respect to Alpine-PV expectations established by prior test-scale experiments and numerical studies. A particular focus is placed on snow-induced losses and snow distribution patterns around the modules, which remain key uncertainties for utility-scale Alpine-PV deployment.

The remainder of this report is structured as follows. Section 2 describes the power plant layout and the monitoring systems. Section 3 presents the power plant status evolution, yield profiles, and key performance indicators. Section 4 addresses snow-related interactions and quantifies induced losses. Finally, Section 5 proposes an empirical model for estimating snow accumulation beneath modules, a critical parameter for Alpine-PV plant design.

2 Site Description

2.1 Location

The Muttsee reservoir is situated in the canton of Glarus, Switzerland. The dam structure is positioned at an elevation of approximately 2500 m a.s.l. (coordinates: E 2'720'684, N 1'191'087 in CH1903+). As shown in Figure 2.1, the PV power plant is installed all along the dam wall. As shown in Figures 2.2 and 2.3, the concrete dam extends approximately 1 km in length and is segmented into 68 numbered blocks of 15 m each, organized into three sectors: the West side, the curve sector, and the East side.

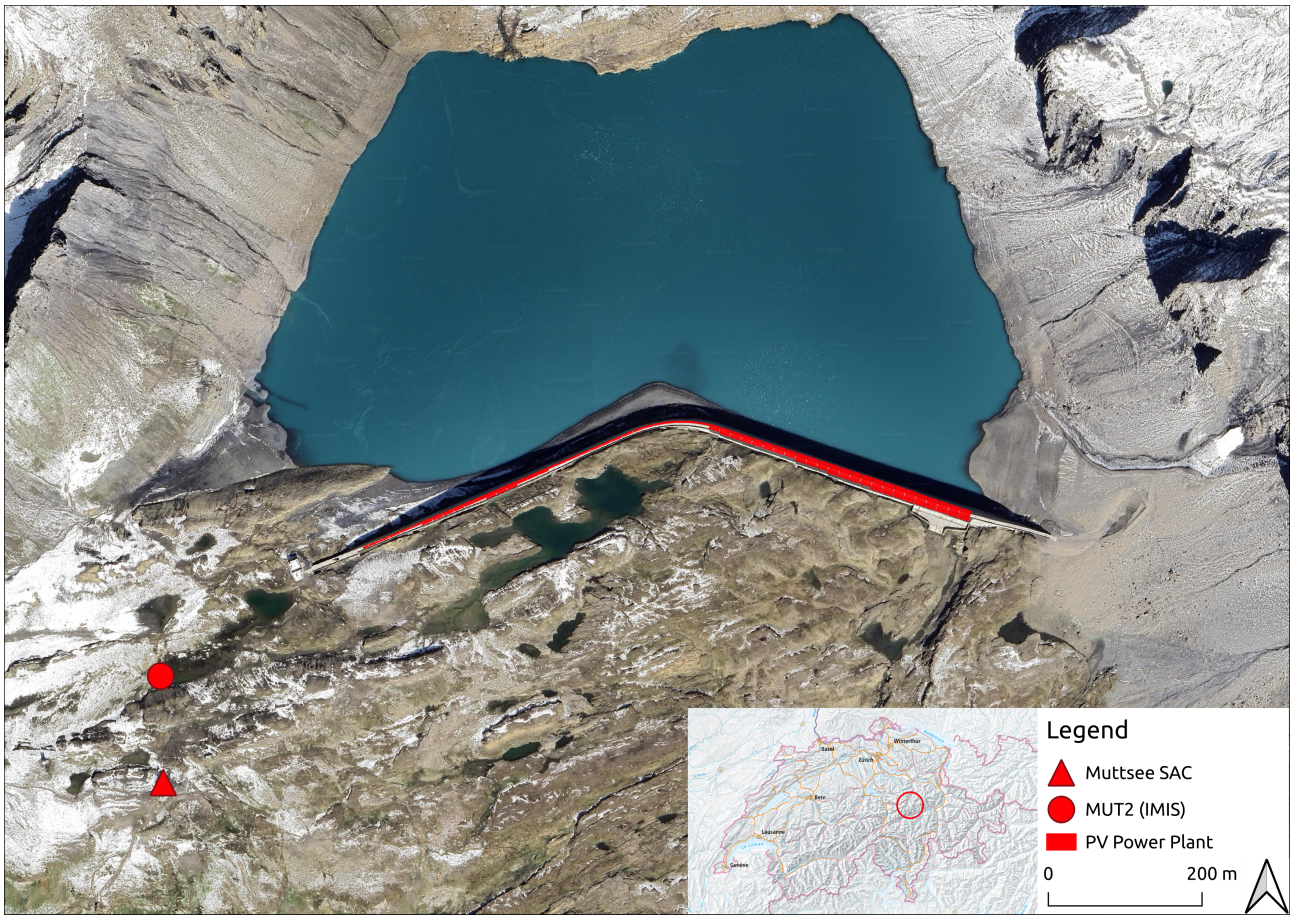


Figure 2.1: *Muttsee reservoir map showing its location above Tierfehd in Glarus, Switzerland. The dam wall is located at approximately 2500 m a.s.l. and extends about 1 km in length. A mountain hut and a measurement station (MUT2) are located nearby. Sources: Google maps (main map), Swisstopo (bottom right map).*

2.2 Power Plant Layout

The Muttsee PV power plant comprises 4875 bifacial modules (Megasol) organized into 232 tables and 23 strings, with a total nominal capacity of 2184 kWp. All modules are mounted on a steel structure attached to the dam wall, leaving a gap between the modules and the concrete surface. The plant employs two module types: a 485 Wp variant (4098 units) and a 385 Wp variant (777 units).

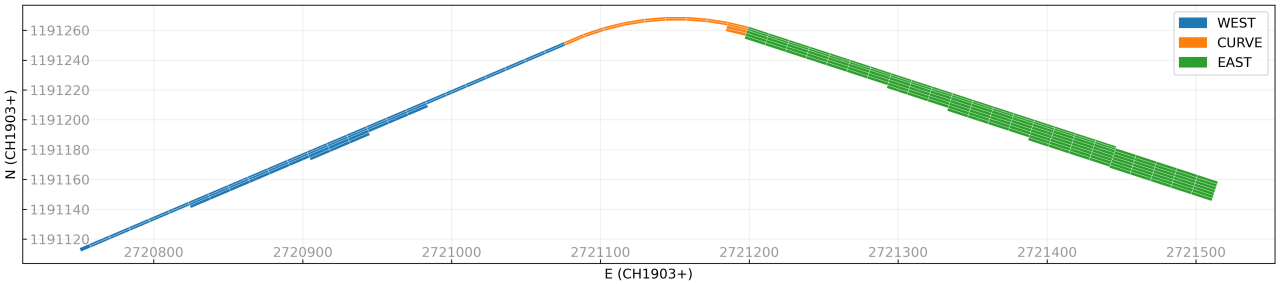


Figure 2.2: *Sectorial plan. The power plant is split in 3 sectors based on the panels orientation.*

The dam geometry imposes constraints on the module orientation, resulting in heterogeneous tilt and azimuth configurations across the plant. Modules are installed at tilts of either 51° or 65°, with the West side facing south-east (azimuth 157°) and the East side facing south-west (azimuth 198°). The curve sector spans intermediate azimuths from 157° to 198° in eight equally spaced steps. Approximately 64% of the installed capacity is oriented at 198°, while 28% faces 157°. The tilt distribution is more balanced, with 56% at 51° and 44% at 65°. Each string feeds into a dedicated inverter (KACO blueplanet 105 TL3, 98.9% efficiency). The combined AC output from all inverters passes through two on-site transformers that step up the voltage from 400 V to 16 kV. The electricity is then transmitted to the valley, where a third transformer increases the voltage to 50 kV for grid injection. Figure 2.3 presents the schematic string plan.

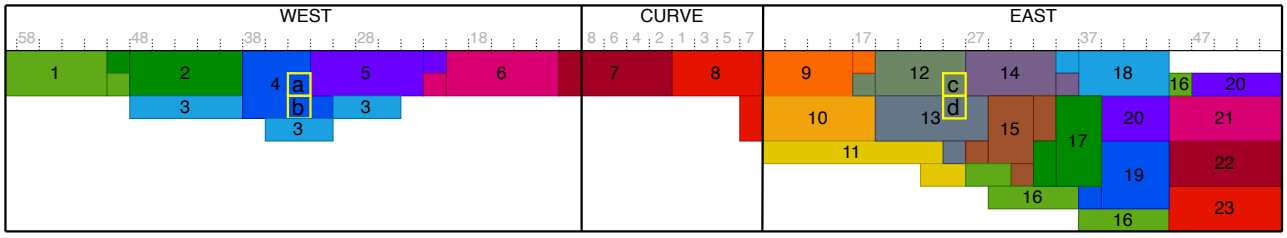


Figure 2.3: *Schematic string plan. Grey numerals indicate block numbers for localization on the dam wall; black numerals indicate string (inverter) numbers. String numbering increases from the West to the East sector.*

2.3 Monitoring Infrastructure

Table 2.1 groups all variables and devices that monitor the Muttsee power plant.

2.3.1 Power variables

The plant is equipped with a supervisory control and data acquisition (SCADA) monitoring system enabling performance analysis at multiple levels of granularity. Power output, including AC- and DC-power, current and voltage, is recorded at the table level via combining string-boxes (only DC) equipped with performance monitoring units (PMUs), and at the string level via inverter PMUs (DC and AC). All measurements are logged at 1-minute resolution by two data loggers and stored on a cloud platform.

Variable	Sensor/Source	Unit	Resolution	Coverage	Availability
Electrical parameters					
DC Power (string)	Inverter PMU	W	1 min	23 strings	from 01.01.2022
DC voltage (string)	Inverter PMU	V	1 min	23 strings	from 01.01.2022
DC current (string)	Inverter PMU	A	1 min	23 strings	from 01.01.2022
AC Power (string)	Inverter PMU	W	1 min	23 strings	from 01.01.2022
AC voltage (string)	Inverter PMU	V	1 min	23 strings	from 01.01.2022
AC current (string)	Inverter PMU	A	1 min	23 strings	from 01.01.2022
DC voltage (table)	String-box PMU	V	1 min	232 tables	from 01.10.2022
DC current (table)	String-box PMU	A	1 min	232 tables	from 01.10.2022
Irradiance					
POA irradiance (front)	Standard cell	W/m²	1 min	4 config.[a]	from 01.10.2022
POA irradiance (rear)	Standard cell	W/m²	1 min	4 config.[a]	from 01.10.2022
Temperature					
Module temperature	Temp. sensor	°C	1 min	4 config.[a]	from 01.10.2022
Imagery					
Panoramic images	Camera system	–	5 min	Plant-wide	Oct–May
Snow height map	Drone survey	m	Annual	Plant-wide	Yearly

Table 2.1: *Summary of measured variables. [a] Four main tilt–azimuth configurations: 51° and 65° tilts at 157° and 198° azimuths.*

2.3.2 Environmental variables

Environmental monitoring includes standard cells for plane-of-array (POA) irradiance measurements and module temperature sensors installed for each of the four main tilt-azimuth configurations (51° and 65° tilts combined with 157° and 198° azimuths). Each configuration is monitored by paired sensors measuring front-side and rear-side irradiance. All sensors are connected to a table-level string-box PMU.
Complete technical specifications for all system components, including PV modules, inverters, transformers, combining string-boxes, and sensors, are provided in Appendix A.
Additionally, as shown in Figure 2.1, the nearby MUT2 measurement station from the Intercantonal Measurement and Information System (IMIS), provides hourly measurement of snow depth and standard meteorological variables (air temperature, wind direction etc). Solar radiation is measured through the reflected shortwave radiation (RSWR), because the pyranometer is placed downwards to avoid snow interference. To compute the incoming shortwave radiation (ISWR), equivalent to global horizontal irradiance (GHI), the ground albedo is necessary and obtained using the SNOWPACK model (Lehning et al., 2002). During periods of intermittent snow cover and in the summer season, albedo values are unreliable and ISWR cannot be computed from RSWR. To circumvent to this common issue of IMIS stations, ISWR measurements from the nearest MeteoSwiss station equipped with a heated pyranometer, Crap Masegn (CMA), are used from May to October included. The CMA station is located at approx. 11 km from the MUT2 IMIS station (E 2'732'824 / N 1'189'378) at approx. the same elevation (2468 m a.s.l).

2.3.3 Camera system

A camera system designed for the Muttsee plant was installed in September 2021 on the Muttsee SAC hut (Figure 2.1). It provides panoramic RGB images of the plant every 5 minutes, from each season's first snow day until the peak of snow accumulation, towards the end of the snow season. As shown in Figure 2.4, images are used to measure the snow accretion and clearing of the PV modules. Due to the interfering topography in

the line of sight of the camera, not all sections of the plant are entirely visible. However, snow accumulation beneath modules can be observed on all three sectors of the plant, at least partially.

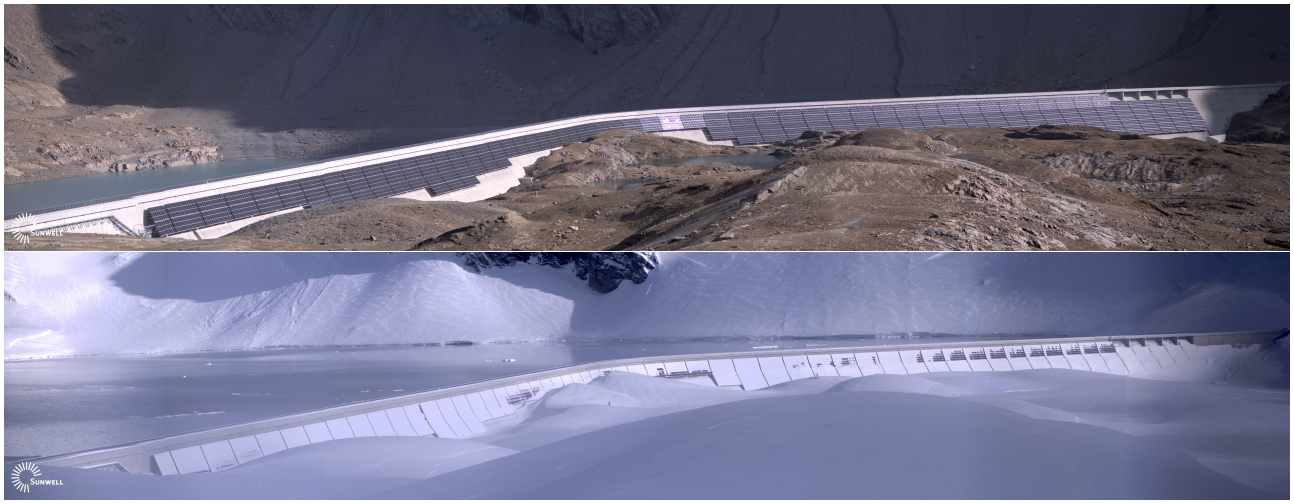


Figure 2.4: *Examples of panoramic images produced by the camera system. Dates: 12.10.2023 (top), 08.01.2024 (bottom)*

2.3.4 Drone surveys

Snow height maps are produced every year at peak elevation using drone-based photogrammetry. By sampling the snow height maps along the bottom of the dam wall, a snow height profile is obtained. Figure 2.5 illustrates the snow height map computation process and presents the 4 snow height profiles measured since 2022. Further details on the different drone surveys, including measurement accuracy, are available in Appendix B.

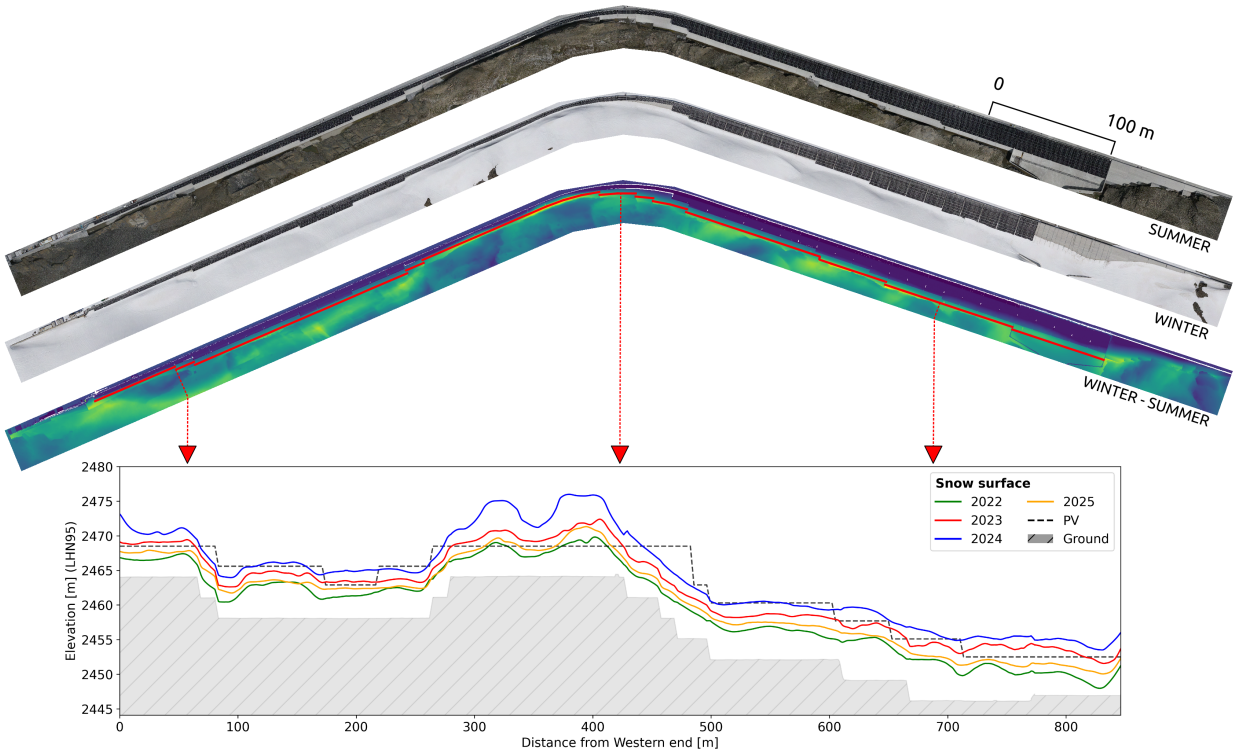


Figure 2.5: *Snow height map computation and resulting profiles. Left: the summer survey (30.08.2022) provides a ground reference elevation; subtracting winter survey elevations yields the snow height map. Right: snow height profiles sampled along the base of the PV modules for each winter survey (20.04.2022, 04.05.2023, 14.05.2024, 04.04.2025). The dashed line indicates the module bottom edge clearance height.*

2.4 Data Availability

The scale of the Muttsee power plant forcibly leads to periods of partial operations, outages and to plant layout modifications. In this section the evolution of the installed power in operation and the associated up-time of the monitoring systems are presented.

2.4.1 Operational timeline and analysis period

The power plant was officially commissioned on the 1st of October 2022, but it was gradually connected to the grid starting late 2021 already and reached the nominal capacity in August 2022. Inverter PMUs were already available during this ramp-up, but not string-box PMUs.
As analyzed in Section 4 below, winter 2023-2024 was exceptionally snowy and led to irreversible damage that caused the shutdown of the plant and a progressive ramp-up in the following months of summer 2024. Some damaged modules were not replaced, leading to a reduction of the nominal power of approx. 9%. The timeline and the corresponding operational installed power are presented in Figure 2.6. Further details on the outage of 2024 and its subsequent progressive ramp-up is provided in Appendix C.
To exploit most of the available data, String analysis is made on the period extending from January 2022 to December 2025, providing 4 full years of measurements. Table-level analysis however starts on 01.10.2022 only, which leaves 3.25 years (3 winters, 3 summers) of measurements.

Measurement Level	Start Date	End Date	Duration
Inverter (string)	01.01.2022	31.12.2025	4 years
String-box (table)	01.10.2022	31.12.2025	3.25 years

Table 2.2: *Analysis periods for each measurement level.*

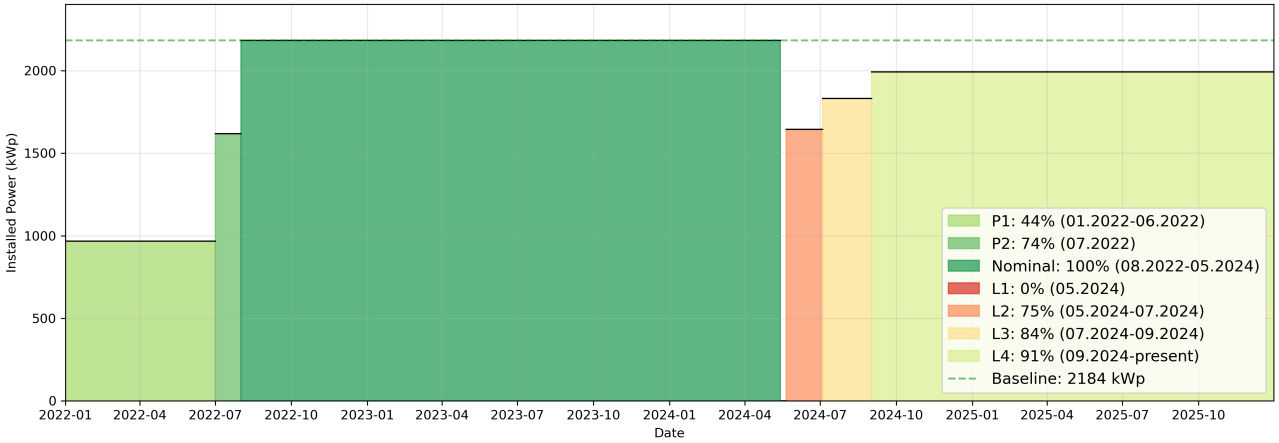


Figure 2.6: *Operational timeline showing installed capacity evolution. Initial ramp-up phase (2021–2022) reached nominal capacity of 2184 kWp in August 2022. Following snow damage in winter 2023/24, the plant underwent shutdown and phased recovery (L1–L4), resulting in permanent capacity reduction to approximately 1990 kWp.*

2.4.2 Monitoring System Uptime

The monitoring infrastructure at Muttsee generates substantial data volumes due to the large number of sensors and the relatively high logging frequency (1-minute resolution at the data loggers). Such systems inevitably encounter failures and outages over extended operational periods. This section presents the availability of the monitoring data and assesses their representativeness for the analyses conducted in this report.

Uptime is computed separately for inverter and string-box PMUs at hourly resolution, considering only devices that were actually installed and commissioned at each time step. To ensure a fair comparison, given that most string-box PMUs power down at night, only daytime timestamps are included in the uptime calculation.

Figure 2.7 presents the monthly uptime values for both measurement levels. String-box PMUs were commissioned later than inverter PMUs (October 2022 versus January 2022), and are therefore not available for the initial months of operation. Table 2.3 summarizes the annual and overall uptime statistics. The notably lower uptime observed in 2024 reflects the plant shutdown and subsequent progressive restart following the snow damage reported in Section 2.4.1.

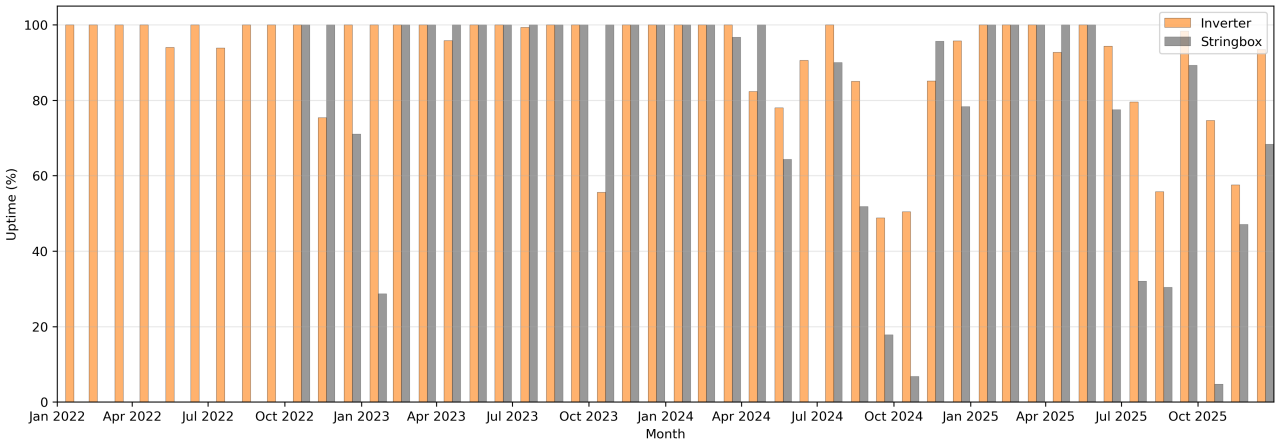


Figure 2.7: *Monthly daytime uptime for inverter (WR) and string-box (SB) PMUs over the analysis period.*

Year	String-box PMU	Inverter PMU
2022	–	97.2%
2023	95.6%	96.2%
2024	64.0%	84.4%
2025	70.1%	87.1%
Overall	**78.6%**	**91.2%**

Table 2.3: *Annual and overall daytime uptime for string-box and inverter PMUs. String-box monitoring was not available (–) in 2022 prior to commissioning in October. Reduced uptime in 2024–2025 reflects plant shutdown and progressive restart following snow damage.*

2.4.3 Camera Time Series

The camera system was operated from the onset of the first snow events in early winter until approximately late April, when peak snow accumulation is typically reached. Although snow events could still occur beyond this period and many panels remained buried, the system was not operated year-round due to technical and logistical constraints. The high-resolution panoramic images produced substantial data volumes that could not be transferred over the cellular network available at the site. Consequently, physical retrieval of the storage disks was required to access the imagery. Since annual drone flights were scheduled at peak snow accumulation to generate snow height maps, the disks were collected during these visits. The storage capacity did not permit continued recording until the following winter season, necessitating system shutdown after each retrieval.

Table 2.4 summarizes the coverage periods for each winter season. In winter 2024/25, the system failed prematurely in late March due to a disk failure, resulting in a shortened observation period.

Season	Start Date	End Date	Duration [days]
Winter 2022/23	24.10.2022	18.04.2023	176
Winter 2023/24	08.10.2023	29.04.2024	204
Winter 2024/25	28.10.2024	23.03.2025	146[a]

Table 2.4: *Camera system coverage periods. [a] Shortened due to disk failure.*

Figures 2.8 and 2.9 present the daily uptime and the monthly mean interval between consecutive images, respectively. The nominal acquisition interval is 5 minutes. Table 2.5 provides seasonal statistics on system availability and temporal resolution. The discrepancy between mean and median image intervals indicates that while the system typically operated at its nominal 5-minute resolution, intermittent outages resulted in occasional longer gaps that inflate the mean interval.

Season	Daytime Uptime	Mean Interval [min]	Median Interval [min]
Winter 2022/23	52.4%	22.5	5
Winter 2023/24	67.1%	15.8	5
Winter 2024/25	75.6%	16.4	5

Table 2.5: *Camera system performance statistics by season. The median interval of 5 minutes corresponds to the nominal acquisition rate; elevated mean intervals reflect intermittent outages.*

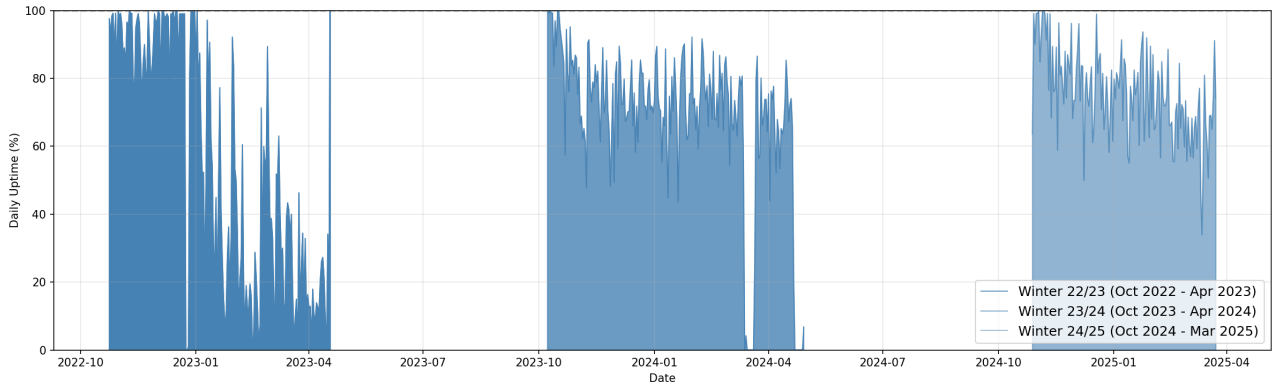


Figure 2.8: *Daily daytime uptime of the camera system across the three monitored winter seasons.*

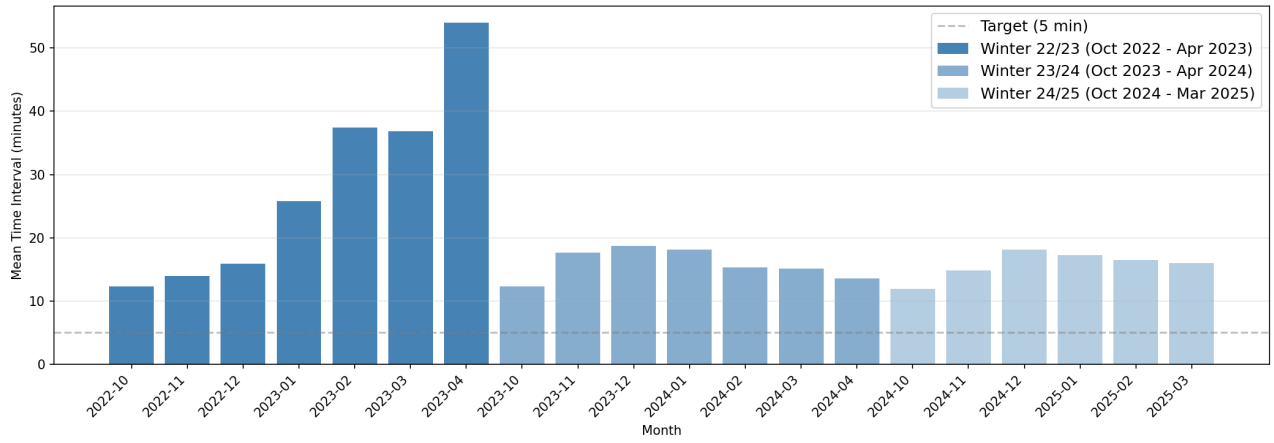


Figure 2.9: *Monthly mean time interval between consecutive images. The dashed line indicates the nominal 5-minute acquisition interval.*

2.5 Data Preprocessing

Raw monitoring data from inverters, string-boxes and meteorological sensors underwent a standardized preprocessing pipeline before analysis. All timestamps were converted to Coordinated Universal Time (UTC) and regularized to uniform 1-minute intervals.

Outlier detection was performed using a quantile-based approach: values falling below the 1st percentile ($q_{0.01}$) or above the 99th percentile ($q_{0.99}$) of each variable's distribution were flagged as outliers and set to `NaN`.

Missing data points were addressed through linear interpolation, with a maximum gap limit of 3 hours (corresponding to 18 consecutive 1-minute intervals). Gaps exceeding this threshold remained as `NaN` values to avoid introducing artifacts from interpolating across extended outages or nighttime periods.

For the string-box data, DC-power (P_{DC}) was computed from the product of measured current (I) and DC-voltage (U_{DC}) for each individual table.

In the end, the 1-minutes measurements were resampled by averaging to 1 hour resolution.

The inverter of the string 18 (WR18) was physically replaced in July 2023. It was treated as a single continuous device by merging data from the original and replacement units at the transition date.

2.6 Meteorological Conditions

Performance assessments of PV power plants require reference meteorological conditions to contextualize measured production. In the following, we compare measured conditions during the reporting period (2022-2025) against historical record (2008-2021) from the nearby IMIS station MUT2.

Overall, the Muttsee PV plant operated from 2022 to 2025 under meteorological conditions representative of the site's long-term climate. Solar irradiance closely matched TMY expectations on average. Snow conditions exhibited high inter-annual variability, with winter 2023-2024 being exceptionally snowy.

2.6.1 Solar Irradiance

Figure 2.10 compares monthly Global Horizontal Irradiance (GHI) for each year of the reporting period against the Meteonorm TMY reference (Remund et al., 2020). Table 2.6 summarizes the annual totals and

deviations from TMY.

Table 2.6: *Annual GHI totals and deviation from TMY reference (1333 kWh/m^2).*

Year	GHI (kWh/m^2)	Deviation from TMY
2022	1391	+4.3%
2023	1339	+0.4%
2024	1250	−6.2%
2025*	1336	+0.2%
4-year mean	**1329**	**−0.3%**

*2025 data through January 14.

The 2022 irradiance exceeded TMY expectations, while 2024 was notably below average (−6.2%). Over the four-year period, the mean GHI closely matches the TMY reference.

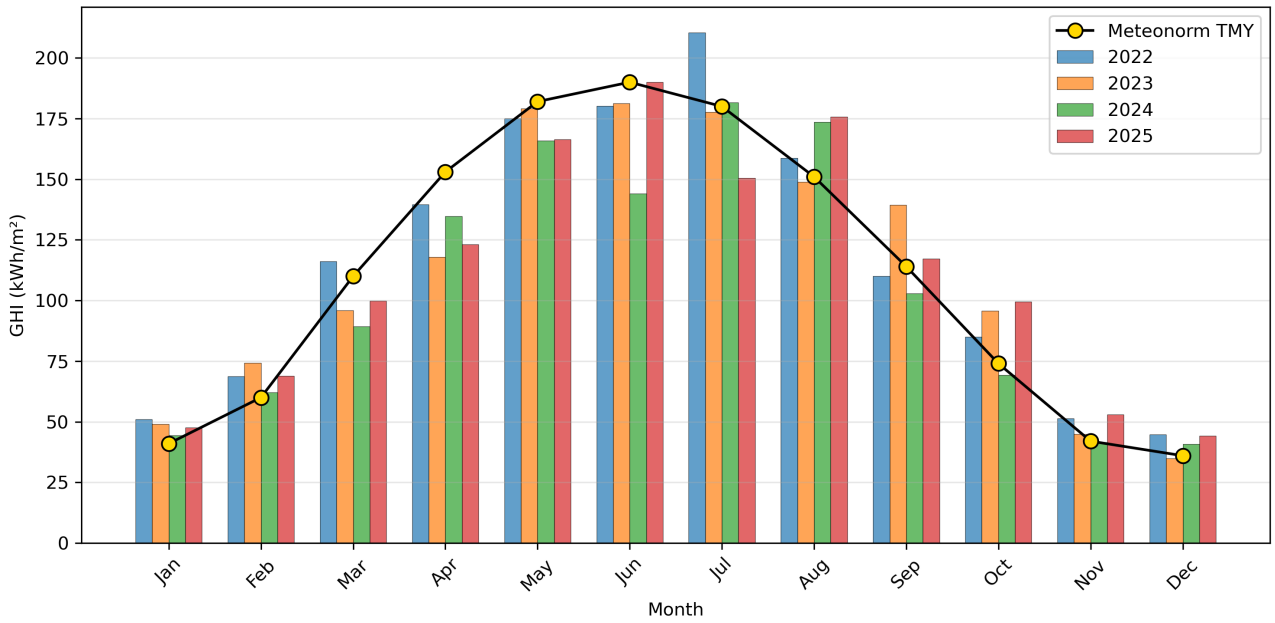


Figure 2.10: *Monthly GHI comparison between measured data (2022–2025) and Meteonorm TMY reference. The TMY line (gold markers) represents typical annual irradiance at the Muttsee site (1333 kWh/m^2/year).*

2.6.2 Snow Cover

Figure 2.11 presents monthly mean snow height, comparing recent years against the 2008–2021 historical record.

The historical record shows peak snow depths in March-April (mean ~260 cm), with complete melt typically occurring by August. The reporting period exhibits substantial inter-annual variability: 2024 experienced exceptionally heavy snow accumulation (peaking above 300 cm in April), while 2022 and 2025 showed below-average snow cover in winter months.

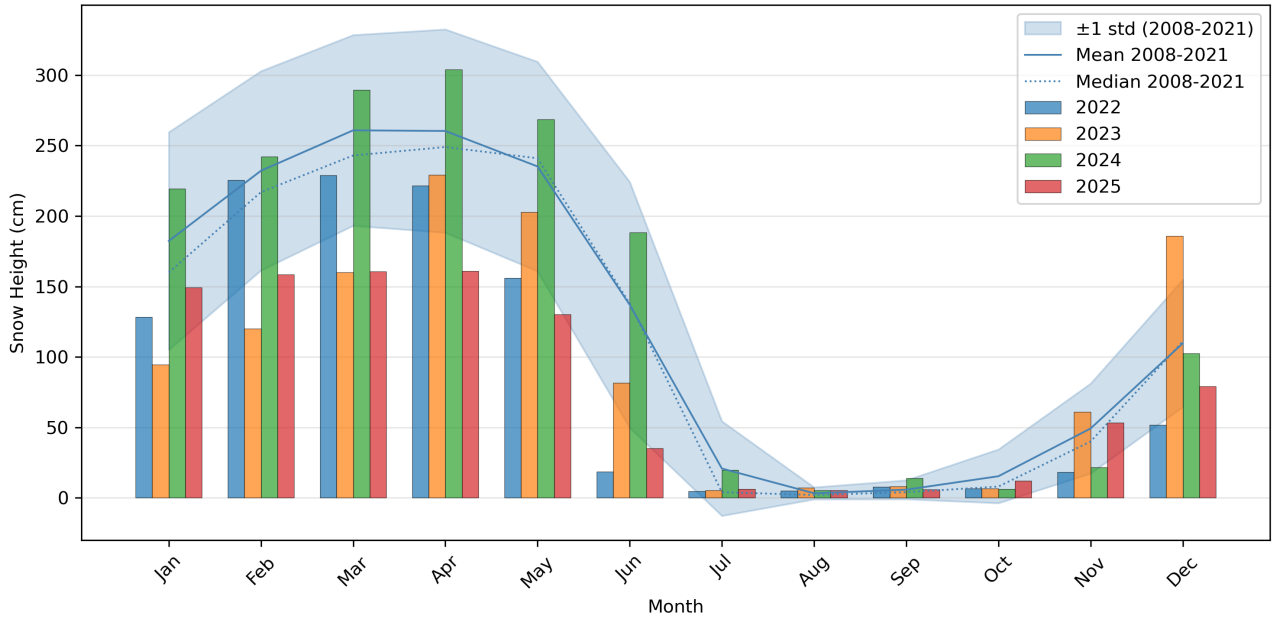


Figure 2.11: *Monthly mean snow height comparison. Historical statistics (2008–2021) shown as mean (solid line), median (dotted), and ±1 standard deviation envelope. Bars indicate measured values for 2022–2025.*

2.6.3 Air Temperature

Figure 2.12 compares monthly mean temperatures during the reporting period against historical statistics. The site experiences alpine conditions with mean temperatures ranging from −7°C in winter to +8°C in summer. The reporting period shows temperatures generally within one standard deviation of historical means.

2.6.4 Wind Speed

Figure 2.13 presents monthly mean wind speeds.
Wind speeds are higher during winter months (mean ~2 m/s) and lower in summer (~1.2 m/s). The reporting period shows wind conditions consistent with historical patterns.

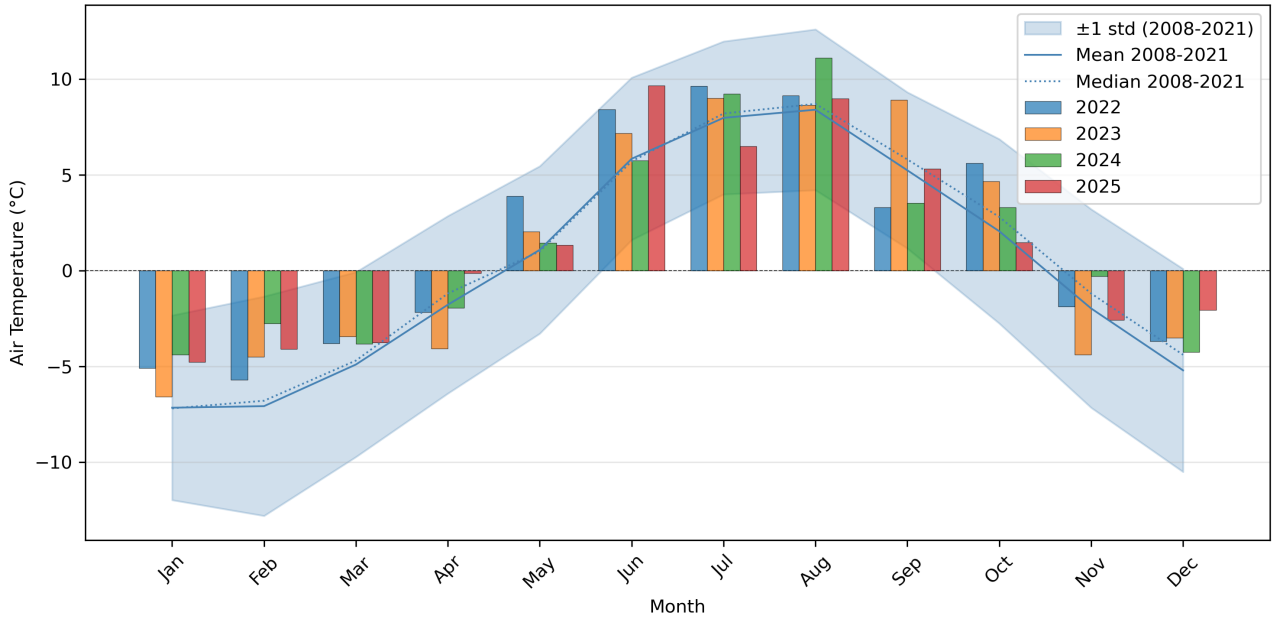


Figure 2.12: *Monthly mean air temperature comparison between the reporting period and historical statistics (2008–2021).*

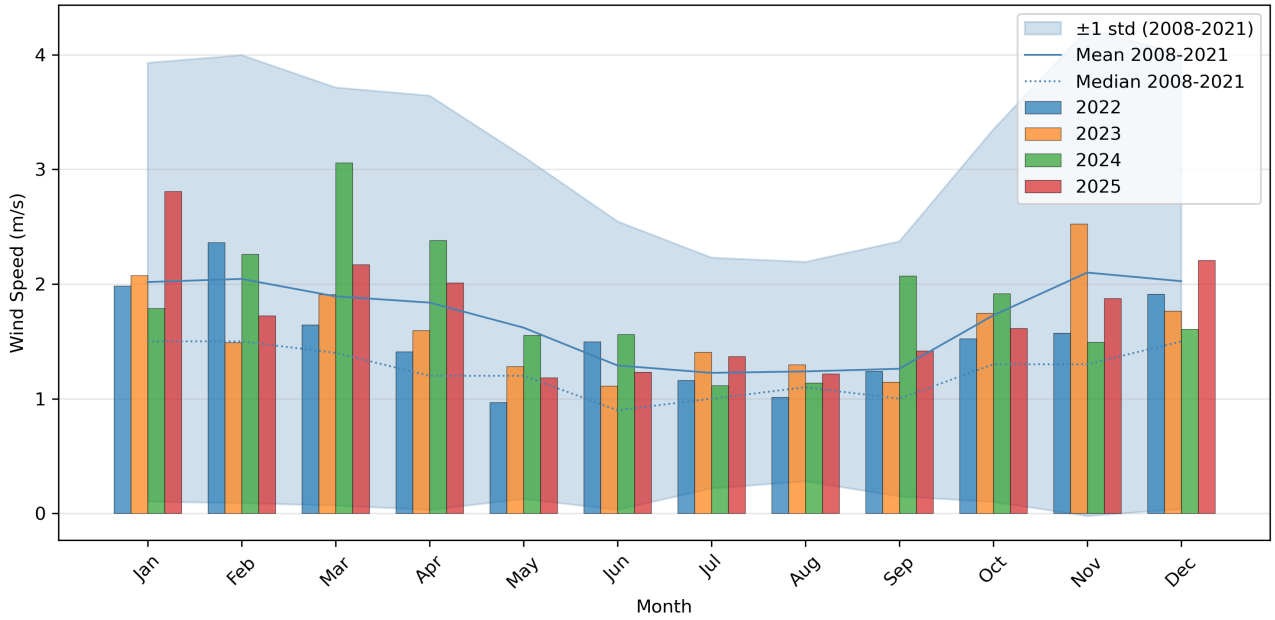


Figure 2.13: *Monthly mean wind speed comparison between the reporting period and historical statistics (2008–2021).*

3 Performance Analysis

3.1 Key Performance Indicators

The final yield (Y_f), also referred to as specific yield, quantifies the efficiency of the installed power capacity:

$$Y_f = \frac{E_{AC}}{P_0} \quad \left[\frac{\text{kWh}}{\text{kWp}}\right] \tag{3.1}$$

where E_{AC} is the AC energy delivered to the grid and P_0 is the nominal installed power. The final yield can be interpreted as the equivalent number of hours during which the PV system operated at its rated capacity.
The capacity factor (CF) is derived directly from Y_f and expresses the ratio of actual production to theoretical maximum production:

$$CF = \frac{Y_f}{T_r} \tag{3.2}$$

where T_r is the number of hours in the period over which Y_f is computed.
The performance ratio (PR) represents the fraction of energy produced relative to the energy an ideal PV cell would generate under the actual irradiance conditions. It is a widely used plant-level metric that aggregates all losses occurring between the available radiative resource and the actual power output, including losses due to wiring, temperature, mismatch, clipping, and other factors:

$$PR = \frac{Y_f}{Y_r} \tag{3.3}$$

where Y_r is the reference yield, which characterizes the plane-of-array irradiance conditions. The reference yield represents the equivalent number of hours at standard test condition irradiance ($G_{0,POA} = 1000\ \text{W/m}^2$):

$$Y_r = \frac{H_{POA}}{G_{0,POA}} \quad [\text{h}] \tag{3.4}$$

where H_{POA} [Wh/m^2] is the time-integrated irradiance in the plane of array.

3.2 Results

Figures 3.1 and 3.2 present the monthly and seasonal final yields, respectively. Seasons are defined according to the Swiss Energy Act: winter spans October through March, and summer spans April through September. Figure 3.3 compares the monthly and seasonal final yield statistics of Muttsee with those of a midland power plant (Payerne) and an Alpine-PV test site (Totalp). This comparison contextualizes the results from Muttsee as a utility-scale Alpine-PV plant alongside the smaller-scale test site, which serves as a reference for expected Alpine-PV yields in terms of both magnitude and seasonal profile. The comparison with the midland power plant, one of the largest free-standing installations in the Swiss Plateau, illustrates the characteristic shift of peak production toward winter in Alpine-PV systems, as well as the increase in both annual yield and winter production share.
The following key observations emerge from these results:

- Muttsee's yield profile conforms to the expectations established by the Totalp test site and theoretical

models (Anderegg et al., 2023; Kahl et al., 2019; von Rütte et al., 2021), with a production peak shifted toward winter and an average winter electricity share approaching 50%.

- The mean annual final yield at Muttsee reaches 1211 kWh/kWp, corresponding to a capacity factor of approximately 13.8%.
- On average, Muttsee annually produced 14.1% more than the midland plant, and the winter production share was 72% greater, confirming the strong advantage of Alpine-PV for winter electricity generation at utility scale.
- During the critical winter months (December–February), Muttsee produced on average 262 kWh/kWp, rising to 288 kWh/kWp when excluding the anomalous 2023/24 season. This represents approximately three times (300%) the yield of the Payerne midland plant (87 kWh/kWp) during the same period. However, Muttsee achieved only 83% resp. 89% of the Totalp test site yield for monofacial modules at comparable tilt (Table 3.2).
- The subsidy threshold established by the Swiss "Solar Express" legislation (500 kWh/kWp in winter) was achieved in two of the three reported winters.
- However, compared to the Totalp test site at a similar tilt (60°), Muttsee yielded 21.6% less annually and 26.7% less in winter. Differences in location, module orientations (not uniformly south-facing at Muttsee), and size effects, notably snow-induced losses (Section 4) and partial system downtimes, appear to have a substantial impact on performance.

Winter 2023/24 was marked by exceptional snow accumulation, as documented in Section 2.6. This led to extended outages and is clearly reflected in the monthly yield profiles, where this season depresses the overall statistics. While these data are retained for completeness in the figures, Table 3.1 provides seasonal and annual performance indicators both with and without the anomalous 2023/24 winter and 2024 summer periods. Table 3.2 extends this comparison to the critical winter months (December–February).

Period	Metric	All Years	Excl. 2024[a]	Difference
Winter (Oct–Mar)	Mean Y_f [kWh/kWp]	524	579	−55
	Mean PR	0.78	0.85	−0.07
Summer (Apr–Sep)	Mean Y_f [kWh/kWp]	668	724	−56
	Mean PR	0.73	0.79	−0.06
Annual	Mean Y_f [kWh/kWp]	1211	1303	−92
	Mean CF	0.138	0.149	−0.011
	Mean PR	0.75	0.79	−0.04

Table 3.1: *Comparison of seasonal and annual performance indicators with and without the anomalous 2024 period. [a] Excludes winter 2023/24 from winter statistics, summer 2024 from summer statistics, and the full 2023/24 year from annual statistics.*

Period	Mean Y_f [kWh/kWp]	All Years (Excl. 2024[a])	Ratio to Payerne
Dec-Feb	Muttsee	262 (288)	3.0 (3.3)
	Totalp mono	314	3.6
	Totalp bi	385	4.4
	Payerne	87	1.0

Table 3.2: *Comparison of high-winter (December–February) final yields across sites. Totalp mono and bi refer to monofacial and bifacial modules at 60° tilt. Payerne represents a midland free-standing installation.* [a] *Excludes December 2023 and January-February 2024.*

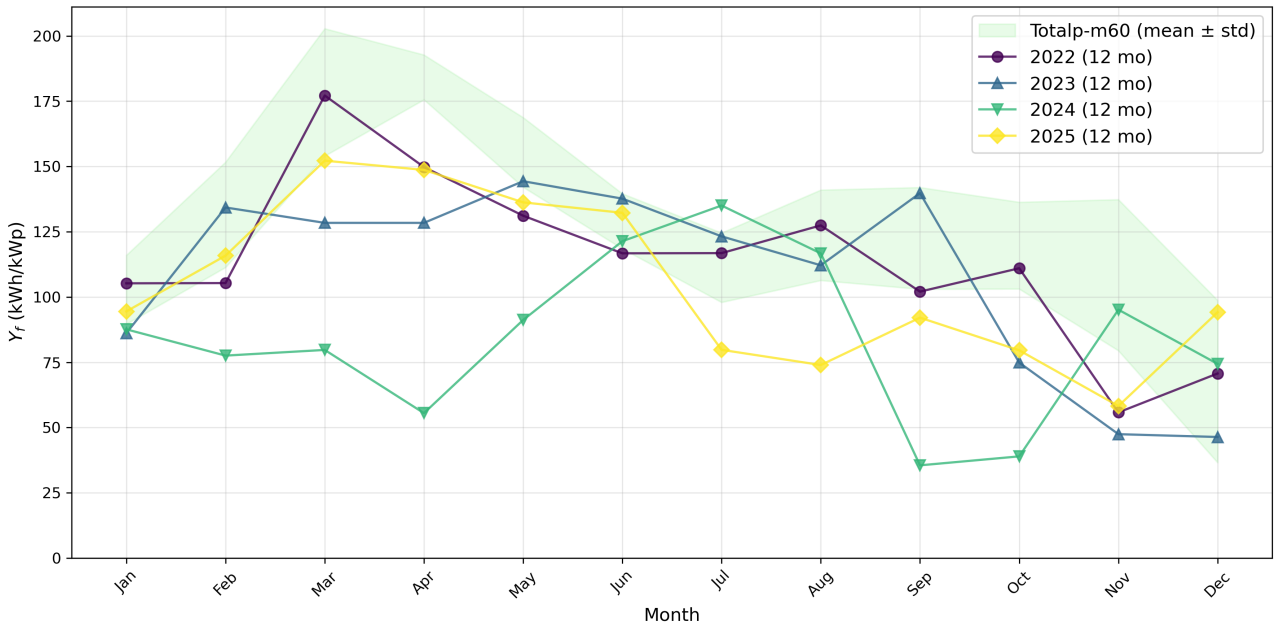


Figure 3.1: *Monthly final yields at Muttsee by calendar year.*

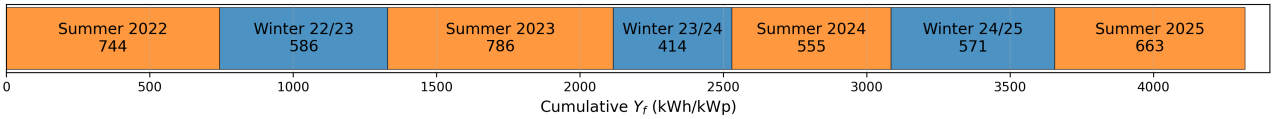


Figure 3.2: *Cumulative seasonal final yields at Muttsee, distinguishing winter (October–March) and summer (April–September) periods.*

The performance ratio (Figure 3.4, left) exhibits notable seasonal and inter-annual variability. Under normal operating conditions, PR values range between 0.77 and 0.88, which is consistent with well-functioning utility-scale PV systems. The anomalous winter 2023/24 and subsequent summer 2024 stand out with significantly depressed PR values of 0.64 and 0.60, respectively, a direct consequence of the extensive snow damage and partial plant shutdown during this period. Excluding this anomalous year, the mean annual PR reaches 0.79 (2023: 0.79, 2025: 0.78), compared to only 0.67 in 2024.

The capacity factor (Figure 3.4, right) follows the expected seasonal pattern for Alpine-PV installations, with winter values that are comparable to or only slightly lower than summer values, in contrast to lowland PV

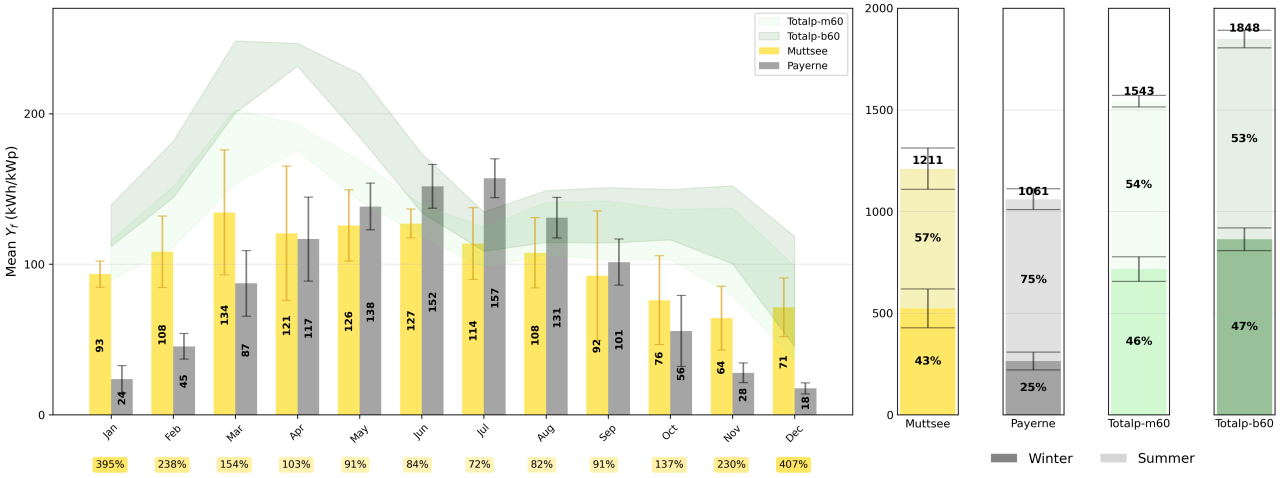


Figure 3.3: *Comparison of monthly and seasonal final yields across three sites: Muttsee (4 years), Payerne midland plant (8 years), and Totalp Alpine-PV test site (5 years). Error bars indicate one standard deviation.*

systems where winter capacity factors are typically 2–3 times lower than summer values. Under normal conditions, seasonal CF ranges from 0.14 to 0.18, corresponding to an annual CF of approximately 14–15%. The winter 2023/24 season recorded a CF of only 0.10, reflecting the combined impact of snow-induced losses and system outages. Annual capacity factors for complete years were 0.16 (2023), 0.13 (2024), and 0.16 (2025), with 2024 again showing the impact of the exceptional snow season.

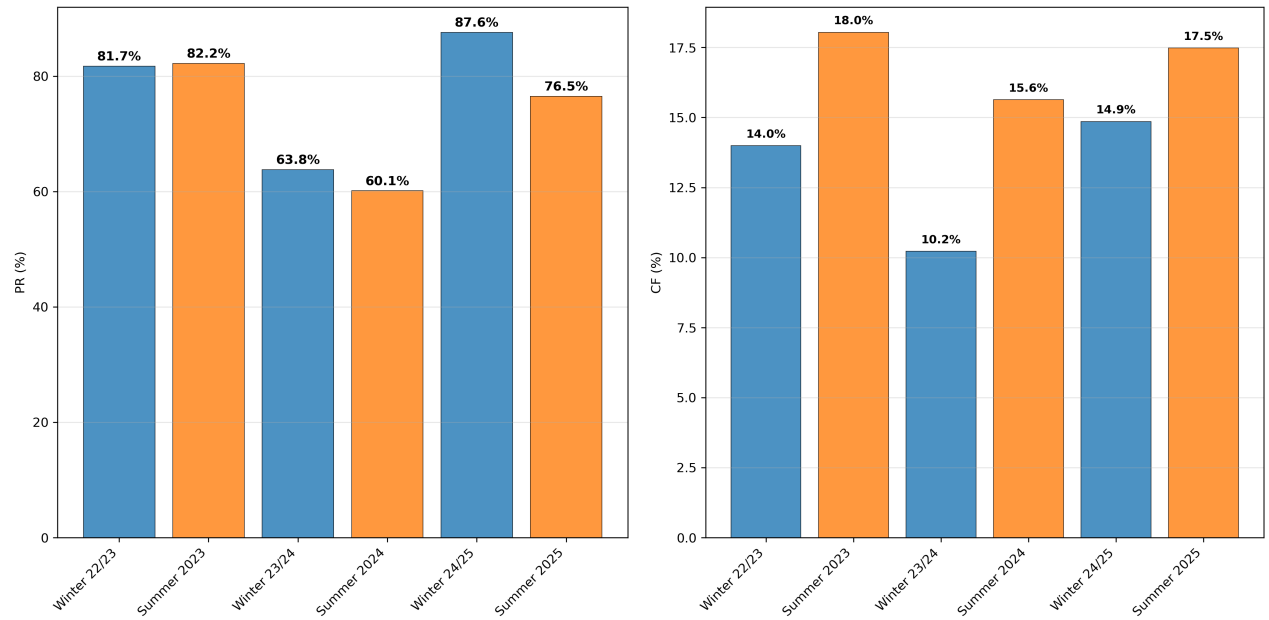


Figure 3.4: *Left: Seasonal performance ratio (PR) over the analysis period. Right: Seasonal capacity factor (CF) over the analysis period.*

Table 3.3 presents the complete seasonal breakdown of all key performance indicators.

Season	Y_f [kWh/kWp]	CF	PR
Summer 2022	744	-	-
Winter 2022/23	586	0.140	0.82
Summer 2023	786	0.180	0.82
Winter 2023/24	414	0.102	0.64
Summer 2024	555	0.156	0.60
Winter 2024/25	571	0.149	0.88
Summer 2025	663	0.175	0.77

Table 3.3: *Seasonal key performance indicators in chronological order. Performance ratio values are capacity-weighted averages across the 51° and 65° tilt configurations.*

4 Snow-Induced Losses

In regions where snow contributes to module soiling, such as Muttsee, snow-induced generation losses can reach 100% during winter months (Pawluk et al., 2019), thereby diminishing the benefits of enhanced snow albedo on power production.
The large variability in reported snow losses stems not only from differences in climatic conditions (Table 4.1), but also from variations in system geometry. Module tilt angle, technology, and layout are key parameters governing observed generation losses, as they control the snow shedding rate (Bogenrieder et al., 2018; Braid et al., 2020). For panel tilts below 10°, melting rather than shedding becomes the dominant clearing mechanism (Andrews et al., 2013), a considerably slower process (Abou Yassine et al., 2022). The clearance height above ground (dashed line in Figure 2.5) also plays a critical role: it determines the potential for interference between snow accumulating beneath the modules and snow deposited on the module surface (Townsend and Powers, 2011). Once the snow pile beneath the panel reaches the module's bottom edge, further shedding is impeded, and snow clearance requires complete melting.
This section presents the snow-induced losses computed for the Muttsee power plant.

Climate	Author	Years	Tilt [°]	Annual Loss [%]	Max. Winter Loss [%]
Mild	Brench (1979)	1978–79	30–40	5–11	–
	Andrews et al. (2013)	2010–12	5–60	1–3.5	–
Moderate	Marion et al. (2013)	2011–13	15–35	1.9–9.3	92
Severe	Townsend and Powers (2011)	2009–11	0–39	6–26	100
	Heidari et al. (2015)	2013–14	0–45	5–34	68

Table 4.1: *Summary of snow losses reported in the literature, classified by climate type following Pawluk et al. (2019).*

4.1 Method

Snow losses are computed by comparing theoretical snow-free electricity production to the actual measured production during snow events. This approach requires plane-of-array (POA) irradiance measurements maintained free of snow, combined with a theoretical PV model. At Muttsee, the POA irradiance sensors are standard cells equivalent to the installed PV modules, which inherently account for all module-related optical and thermal losses. This simplifies the PV model to:

$$P_{DC,th}(\phi,\theta) = G_{POA}(\phi,\theta) \cdot A_{PV} \cdot \eta_{PV} \quad [\mathrm{W}] \tag{4.1}$$

where G_{POA} [W/m^2] is the plane-of-array irradiance measured by the standard cells, ϕ and θ are the azimuth and tilt angles respectively, A_{PV} [m^2] is the total module area, and η_{PV} is the module efficiency under standard test conditions.
Snow loss is then computed as:

$$P_{DC,loss} = P_{DC,th} - P_{DC,meas} \tag{4.2}$$

where $P_{DC,meas}$ is the table-level DC power derived from the current and voltage measurements recorded by the string-box PMUs.
Since no dedicated G_{POA} measurement is available for modules in the curve sector, the average of the East and West sector measurements at the corresponding tilt is used as a proxy. The placement of the standard cells between module tables, combined with their relatively small surface area, ensured that snow did not accumulate on their sensing surface. A comparison with GHI measurements from the nearby MUT2 station during snow events confirmed no anomalous deviations attributable to snow coverage of the sensors.

4.1.1 Snow Event and Interference Detection

Snow events were identified using the panoramic image time series from the camera system. All available images were visually inspected, and the start and end dates of snow events were manually recorded. A total of 106 events were detected across three winters. Figure 4.1 presents their temporal distribution and duration. The complete list of events is provided in Appendix D.

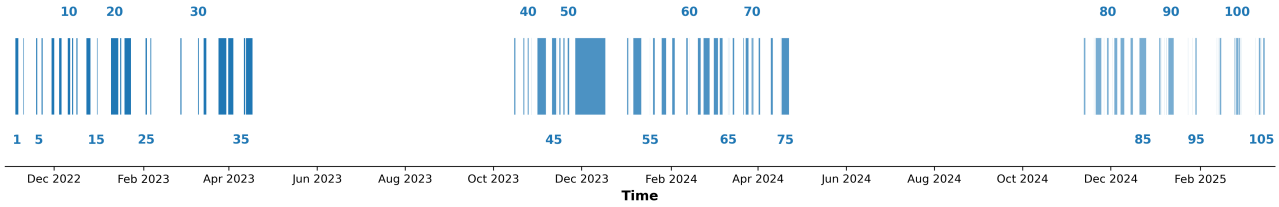


Figure 4.1: *Temporal distribution and duration of snow events across the three monitored winter seasons.*

Nighttime conditions and adverse meteorological visibility did not always permit observation of the modules at the precise onset of snow accretion. Consequently, the recorded start of a snow event corresponds to the first visible evidence of snow presence on the modules, which may be slightly delayed relative to the actual onset, either due to darkness or ongoing snowfall. In both cases, irradiance levels are very low, and the equivalent unrecorded time contributes negligibly to the integrated loss estimate.
The end of an event was recorded when all modules across the plant were visually cleared. This definition implies that an event may include time steps during which most modules have already been snow-free for some time while only a few retain residual snow patches. As a consequence, two distinct snow accumulation episodes may be grouped into a single recorded event. This occurred, for instance, during the longest event observed, event 51, which spanned three weeks between November and December 2023.
Snow interference, defined as the condition where accumulated snow beneath the modules reaches the bottom edge of the lowest panels, was recorded using a binary flag for each of the three plant sectors, as illustrated in Figure 4.2. The flag was set to true when visual inspection confirmed that the sub-module snow height had reached the panel edge, and reset to false when subsequent observations indicated the snow level had receded.

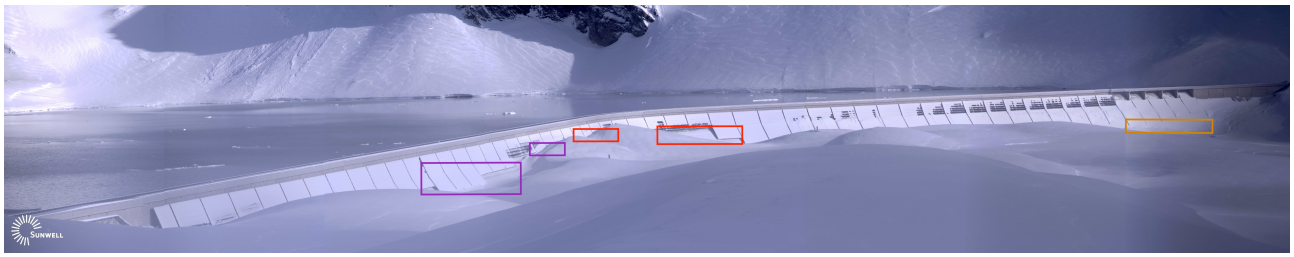


Figure 4.2: *Locations on the panoramic images where interference was observed, with at least one observation point per sector. Purple: West sector, Red: Curve sector, Orange: East sector.*

4.1.2 Interference-Induced Losses

Interference leads to module burial, as snow accumulating on the module surface can no longer shed. The resulting losses are therefore prolonged and continuous, in contrast to the typically brief losses induced by snow that eventually slides off. Accordingly, interference-induced losses were computed continuously from the moment an interference flag was activated until it was deactivated, disregarding the nominal end date of the associated snow event, and only for the lowest tables of modules in the East and West sectors. In the curve sector, all modules were considered (Figure 4.3).
In cases where the interference flag remained active at the final record of a season, it was virtually maintained until the snow height measurement from the nearby MUT2 station fell below 1 m. This approach enables the estimation of interference-induced losses beyond the end of the image time series without imposing overly restrictive assumptions. Conversely, snow events were not synthetically generated after the conclusion of the image record, although a small number of late-season events may consequently have been missed.

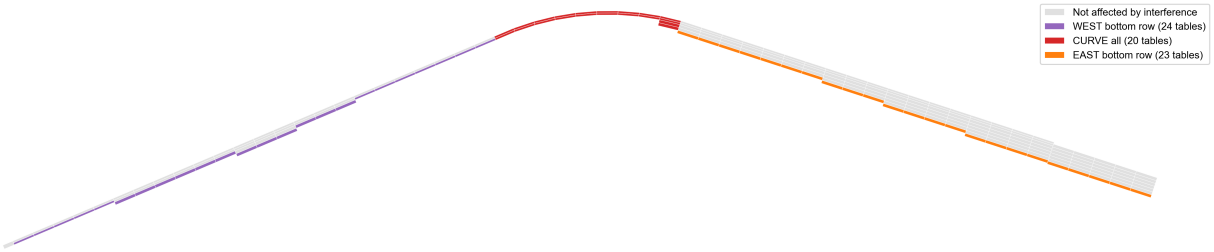


Figure 4.3: *Module tables included in the interference-induced loss computation for each sector.*

4.1.3 Correction for Outages in 2024

As detailed in Section 2.4.1, the exceptional snow accumulation during winter 2023/24 led to structural damage requiring a full plant shutdown in May 2024, followed by a phased recovery extending into autumn. During this period, some PV modules were removed and not replaced, permanently reducing the installed capacity.
Outage-induced losses were computed separately from snow event losses and can subsequently be aggregated to obtain the total snow-attributable generation deficit. The methodology employs the weekly final yield (Y_f, in kWh/kWp) measured at string level (WR) during the reference year 2023, as shown in Figure 4.4, multiplied by the impacted installed capacity during each outage phase.

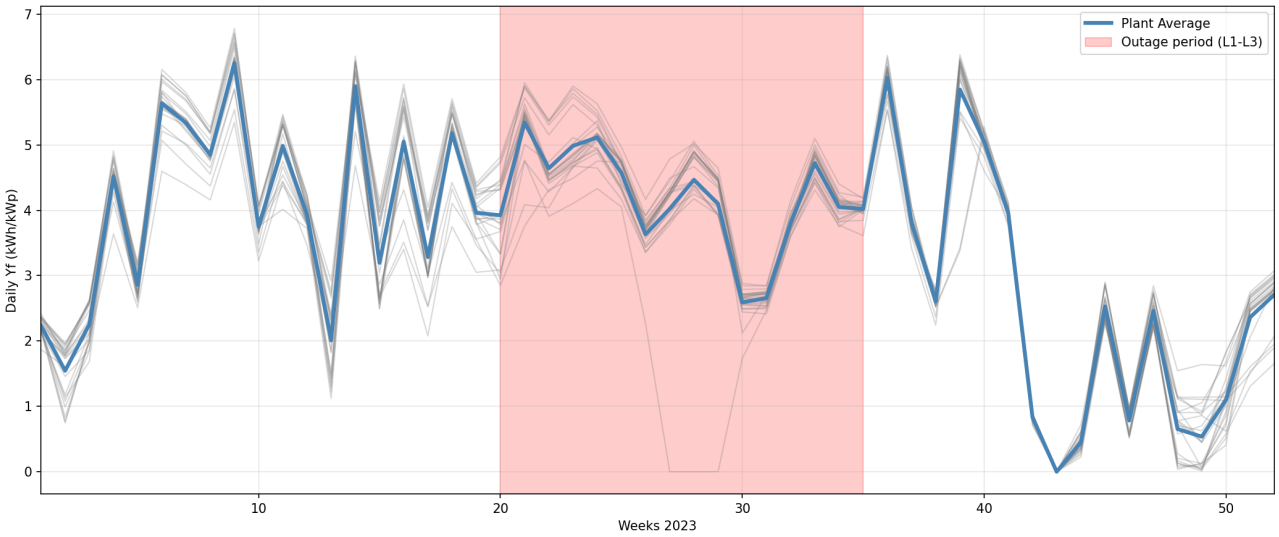


Figure 4.4: *Weekly final yield per string during 2023, used as reference for outage loss estimation.*

Four distinct outage phases were identified based on the operational status of each string (Table 4.2). Phase L1 corresponds to the complete plant shutdown immediately following the damage assessment. Phases L2 and L3 represent progressive recovery as undamaged strings were reconnected. Phase L4 reflects the permanent state following removal of damaged modules.

Phase	Period	Days	Loss [MWh]
L1	14.05.24 – 21.05.24	0	63.6
L2	21.05.24 – 04.07.24	12	106.2
L3	04.07.24 – 01.09.24	13	76.5
L4	01.09.24 – 30.06.25	302	187.9
Total (L1–L4)			434.2

Table 4.2: *Outage phases following the winter 2023/24 snow damage. "WRs offline" indicates strings completely disconnected; "WRs partial" indicates strings operating at reduced capacity due to removed modules.*

For the purpose of attributing losses to snow, only phase L2 is added to the loss estimate. During phase L1, table-level (SB) monitoring remained operational, i.e. irradiance sensors where still measuring, such that losses during this period are already captured by the method based on detected snow events and interference. The SB monitoring outage began precisely at the start of phase L2, necessitating the use of string-level (WR) reference yields for loss estimation from that point onward. Phase L3 began in July 2024, after snow heights had fallen below the 1 m interference threshold, and thus represents maintenance-related rather than snow-induced losses. Phase L4 reflects the permanent capacity reduction and is accounted for by adjusting the nominal installed power from season 2024/25 onward (see Appendix C).

4.2 Results

Snow-induced losses, disaggregated by mechanism (shedding snow versus interference-induced burial), are presented as daily time series in Figure 4.5 and aggregated by season in Figure 4.6.

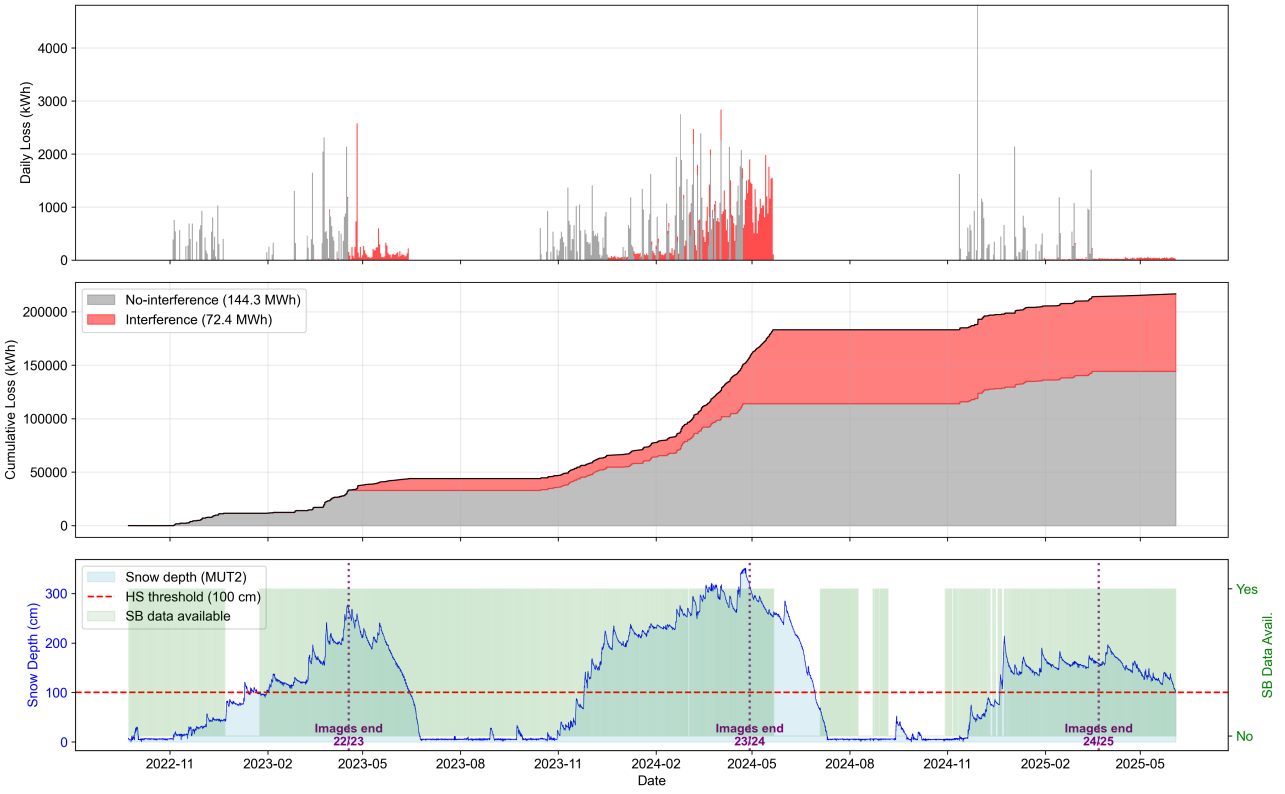


Figure 4.5: *Daily snow-induced losses over the three monitored seasons, showing contributions from shedding snow (top) and interference-induced burial (bottom).*

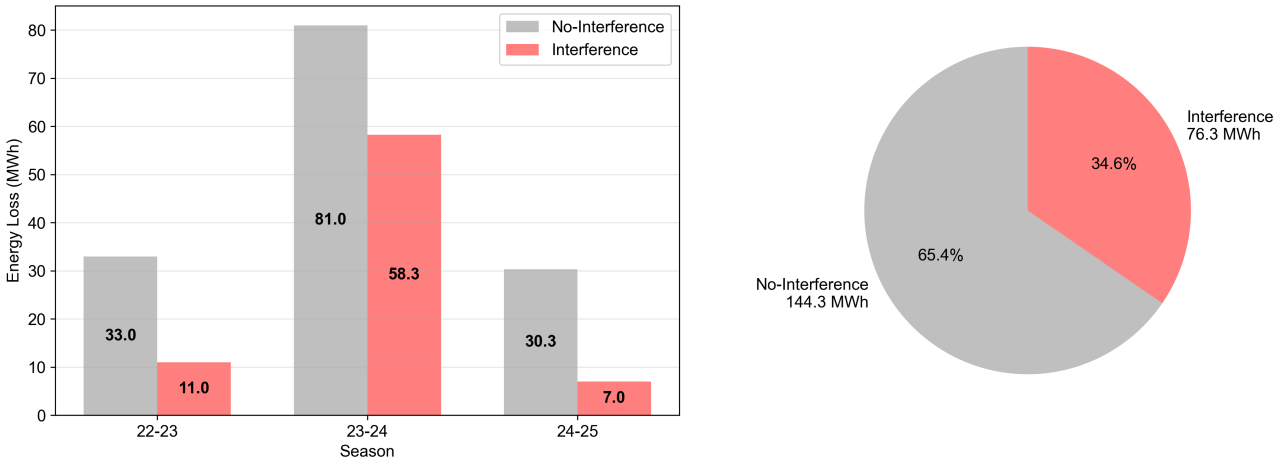


Figure 4.6: *Seasonal snow-induced losses split by mechanism.*

Table 4.3 summarizes the snow losses across the three monitored seasons without considering outage losses. The total measured loss reached 220.6 MWh, with shedding-related losses (no interference) representing approximately two-thirds of the total. The 2023/24 season exhibited exceptionally high losses due to prolonged interference conditions, with interference-induced losses accounting for 41.9% of the seasonal total compared to an average of 22% for the other two seasons.

Season	No-interf. [MWh]	Interf. [MWh]	Total [MWh]	Loss [%]	Interf. share [%]
2022/23	33.0	11.0	44.0	2.7	25.0
2023/24	81.0	58.3	139.3	13.3	41.9
2024/25	30.3	7.0	37.3	2.5	18.8
Total	144.3	76.3	220.6	–	34.6

Table 4.3: *Snow losses by season and mechanism without considering outages period L2. Loss percentage is relative to theoretical production during the period used for snow loss computation. Interference share indicates the proportion of seasonal losses attributable to module burial.*

Gaps in table-level (SB) monitoring data, notably during January 2023 and from late May to July 2024 (Figure 4.5), precluded loss computation during these periods. Consequently, the estimates represent lower bounds on the true snow-induced losses. The summer 2024 data gap begins at the start of outage phase L2, while phase L1 losses are captured in the computation based on snow events and interference. The separate outage loss quantification is presented in Table 4.2.
Table 4.4 presents the total snow-attributable losses for season 2023/24, incorporating the outage phase directly caused by snow damage. Adding phase L2 yields a total of snow-induced losses of 245.5 MWh for the season, with interference-related losses (including outage) representing 67.0% of the total.

Loss component	2023/24 [MWh]	Share [%]
Shedding snow	81.0	33.0
Interference	58.3	23.7
Outage L2	106.2	43.3
Total snow-attributable	245.5	100.0
of which interference-related	*164.5*	*67.0*

Table 4.4: *Total snow-attributable losses for season 2023/24, including losses computed based on detected snow events and interference, and outage phase L2. Interference-related losses include interference detected on images and the L2 outage phase.*

Excluding the 2023/24 season, anomalous for its snow conditions, the mean annual snow loss at Muttsee was 40.7 MWh, corresponding to 2.6% of theoretical production during the analysed period and 1.4% of mean annual production (Table 3.1). Interference contributed 22% of these losses on average. Including all three seasons, mean annual snow losses rise to 73.5 MWh (2.8% of mean annual production).
The 2023/24 season alone accounted for 139.3 MWh in losses without outage considerations (4.9% of reference annual production), rising to 245.5 MWh when including the L2 outage phase (8.6%). This anomalous season represents an extreme event attributable to exceptional snowfall. The disproportionate share of interference-related losses in 2023/24 (41.9%) compared to other seasons (22%) underscores the critical importance of sub-module clearance height in Alpine-PV plant design: when appropriately dimensioned, snow losses remain modest, but once the interference threshold is reached, consequences become severe.

5 Modeling Interference Height

As demonstrated in the previous section, the interference height beneath PV modules is a critical design parameter for Alpine-PV power plants. Using the four drone-based snow height measurements, this section proposes an empirical model to estimate this parameter based on local topography, snow climatology, and plant geometry.

5.1 Background

Townsend and Powers (2011) proposed a simplified geometric relationship between interference height and plant geometry, illustrated schematically in Figure 5.1. In this theoretical framework, the module width is assumed infinite, and shedding snow accumulates on the ground in a triangular cross-section, termed the dissipation zone. This zone is defined by the drop height H (vertical distance from the module's bottom edge to the ground) and the angle of repose α, which characterizes the slope of the accumulated snow pile. The angle of repose depends on internal snow friction and varies with air temperature, drop height, and particle diameter (Eidevåg et al., 2022).
The modeling approach of Townsend and Powers (2011) is based on mass conservation: shedding snow and direct precipitation are incrementally added to the dissipation zone until its capacity is exhausted, at which point interference occurs.
The dissipation zone cross-sectional area A is defined as:

$$A = \frac{W \times H}{2} = \frac{H^2}{2\tan(\alpha)} \tag{5.1}$$

where the base width W is:

$$W = \frac{H}{\tan(\alpha)} \tag{5.2}$$

The interference criterion accounts for both ground snow accumulation h_g and shedding snow. The residual dissipation capacity A' after ground snow accumulation is:

$$A' = \frac{(H - h_g)^2}{2\tan(\alpha)} \tag{5.3}$$

The cross-sectional area of shedding snow A_s depends on the snow depth on the panel h_p and the panel slant length L:

$$A_s = h_p \times L \tag{5.4}$$

Interference occurs when the shedding snow exceeds the residual dissipation capacity:

$$\text{Interference} = \begin{cases} \text{true} & \text{if } A_s \geq A' \\ \text{false} & \text{otherwise} \end{cases} \tag{5.5}$$

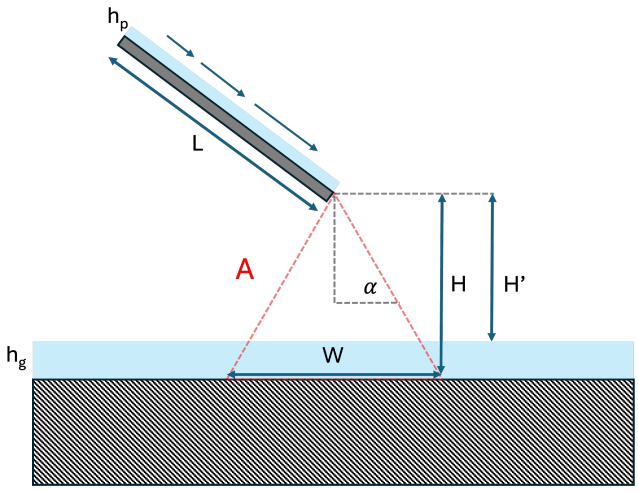


Figure 5.1: *Schematic cross-section of the interference model geometry, adapted from Townsend and Powers (2011). The dissipation zone (area A) is defined by the drop height H and angle of repose α. Ground snow accumulation h_g reduces the available dissipation capacity to A'. Interference occurs when accumulated shedding snow A_s exceeds A'.*

5.2 Model Development

To estimate the maximum snow height accumulation beneath the modules (HS_{PV}^{max}) for a given location and power plant geometry, we adapt the framework of Townsend and Powers (2011). The drone-based measurements of maximum accumulation presented in Figure 2.5 serve as the target variable, shown as snow height (snow surface minus ground surface) in Figure 5.3.

5.2.1 Model Parameters

The dissipation zone is computed based on the drop height (dashed line in Figure 2.5) and corrected for local topography using a high-resolution digital elevation model, as illustrated in Figure 5.2. The ratio of the topography-informed dissipation zone (A') to the idealized dissipation zone (A), computed with $\alpha = 40°$ as in Townsend and Powers (2011), termed the dissipation ratio (ϕ_d), quantifies the extent to which local terrain geometry alters the theoretical dissipation capacity.
The projected panel slant length (L_{PV}^{proj}) serves as a proxy for the volume of shedding snow that fills the dissipation zone. This parameter exhibits substantial heterogeneity along the Muttsee dam, providing considerable variability in the dataset. Figure 5.3 presents both the dissipation ratio and projected slant length profiles alongside the measured snow heights.
Local snow climatology is parameterized using the seasonal maximum snow height (HS_{STN}^{max}) recorded at the nearby IMIS ground station on flat terrain. An alternative parameter, the cumulative seasonal snow precipitation (HS_{STN}^{cum}), was also considered. The measured snow height profiles represent aged snowpacks that have undergone settlement and metamorphism. The maximum snow height parameter implicitly incorporates these processes, whereas cumulative precipitation does not.

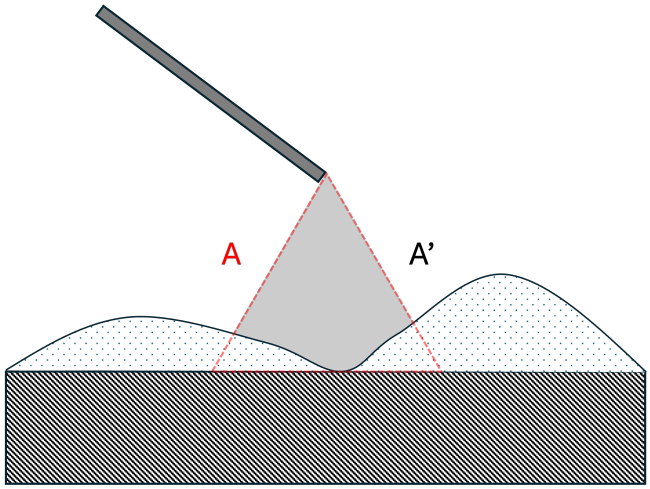


Figure 5.2: *Topography-corrected dissipation zone geometry. Local terrain slope and elevation variations modify the idealized triangular dissipation zone, yielding the effective dissipation area A'.*

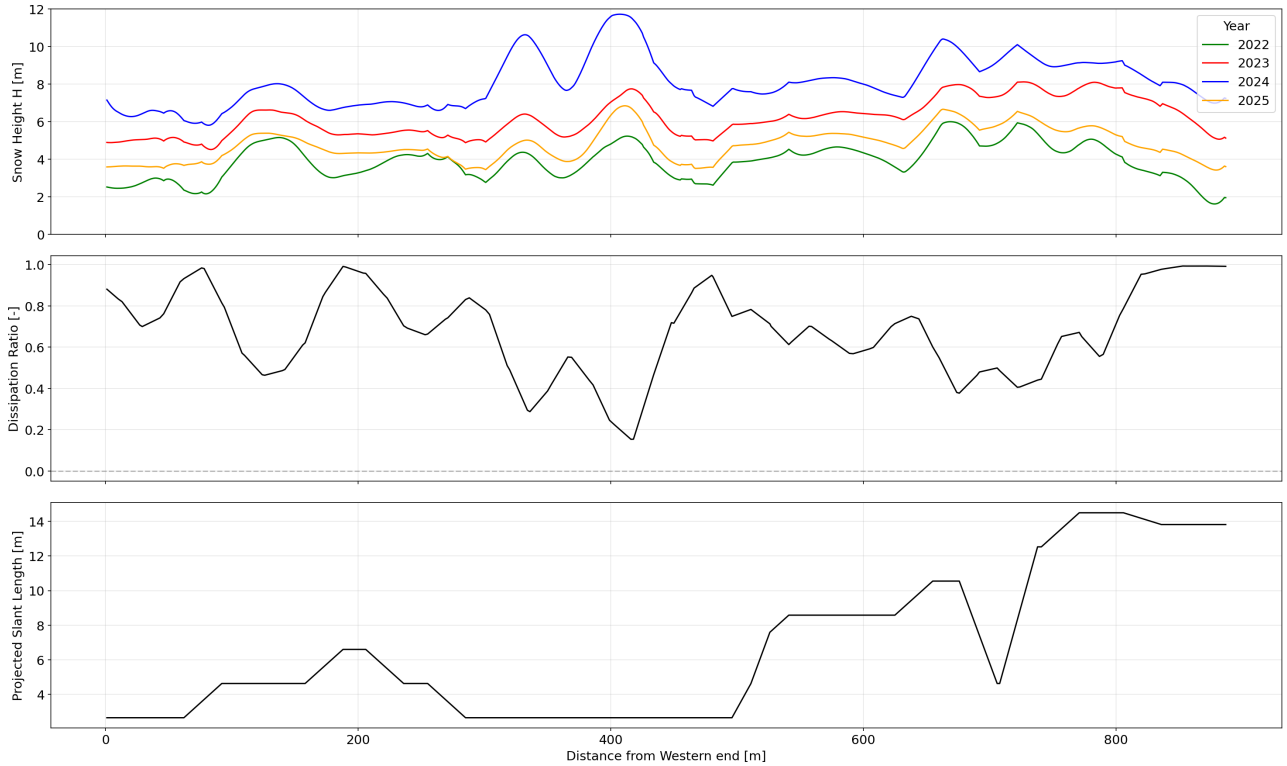


Figure 5.3: *Spatial profiles along the dam for each survey year. Top: measured snow height beneath modules (HS_{PV}^{max}). Middle: dissipation ratio (ϕ_d). Bottom: projected panel slant length (L_{PV}^{proj}).*

5.2.2 Principal Component Analysis

A principal component analysis (PCA) was performed on the correlation matrix of the candidate predictor variables. The correlation matrix and resulting biplot are presented in Figure 5.4.
The first principal component (PC1) explains 40.2% of the variance. The clear separation of 2024 from other

years along this axis, combined with the strong loading of all snow height parameters, confirms both the importance of snow climatology and the exceptional nature of the 2023/24 winter. The parameters HS_{STN}^{max} and HS_{STN}^{cum} overlap substantially, indicating strong mutual correlation and similar predictive relationships with the target variable HS_{PV}^{max}.
The second principal component (PC2) explains 25% of the variance. The parameters ϕ_d and A are correlated along this axis, with ϕ_d exhibiting slightly higher loadings on both PC1 and PC2. The projected slant length (L_{PV}^{proj}) aligns primarily with PC2 but shows moderate loading; however, it dominates PC3 with a loading of 0.89, indicating that it captures variance orthogonal to the other predictors. Complete PCA results, including loadings, cumulative variance explained, and Kaiser and broken stick criteria, are provided in Appendix E.

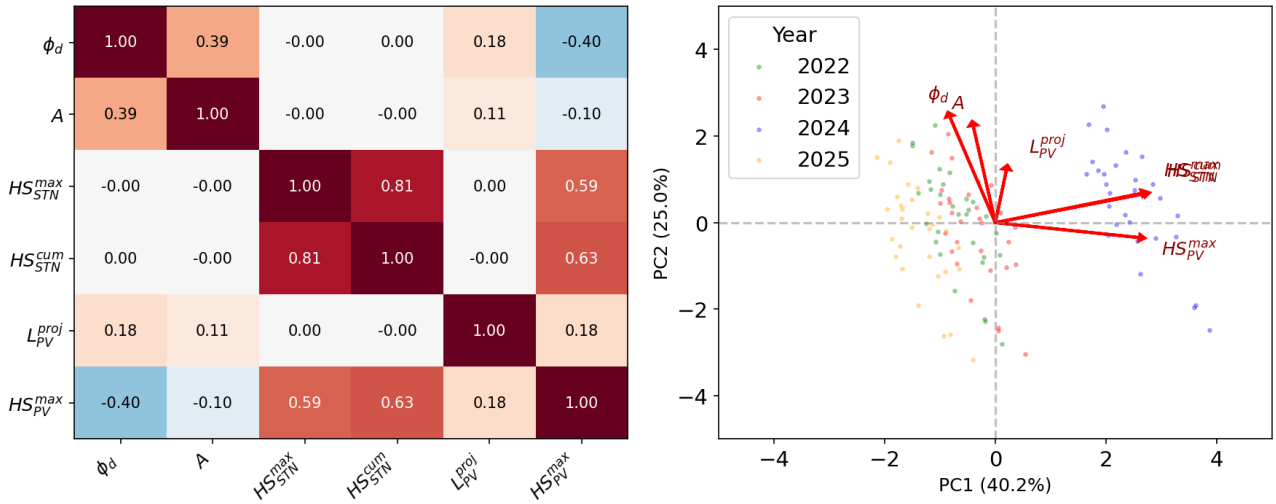


Figure 5.4: *Left: correlation matrix of candidate predictor variables and target (HS_{PV}^{max}). Right: PCA biplot showing variable loadings on PC1 and PC2, with observations colored by survey year.*

5.2.3 Linear Model

Based on the PCA results, the following linear model is proposed:

$$HS_{PV}^{max}[m] = a \cdot \phi_d + b \cdot HS_{STN}^{max} + c \cdot L_{PV}^{proj} + d \tag{5.6}$$

The parameter HS_{STN}^{max} is retained over HS_{STN}^{cum} for practical convenience, as maximum snow height is more readily available from standard meteorological observations.

5.3 Results

Model parameters were estimated using ordinary least squares regression. Two model fits are presented: one including all years and one excluding 2022, which appeared as an outlier in predicted values and reduced the overall coefficient of determination (Figure 5.5). Parameter estimates for both fits are provided in Table 5.1.

Parameter	All years (2022–2025)	Excl. 2022 (2023–2025)
a (dissipation ratio) [m]	4.209	4.254
b (max. snow height) [–]	0.024	0.024
c (proj. slant length) [–]	1.799	1.968
d (intercept) [m]	−3.113	−2.695
R^2	0.587	0.889
RMSE [m]	1.23	0.58
MBE [m]	0.00	0.00

Table 5.1: *Fitted model parameters and performance metrics for both model configurations. Including 2022 reduces model performance ($R^2 = 0.59$) compared to excluding it ($R^2 = 0.89$), suggesting anomalous conditions during the first survey year.*

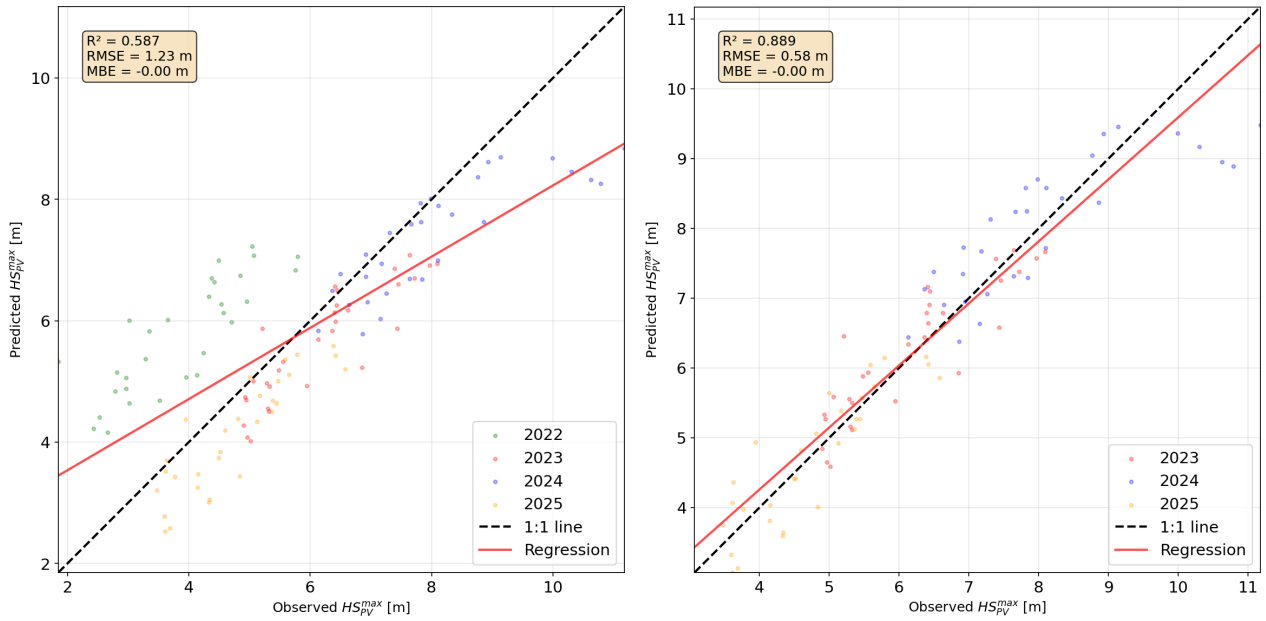


Figure 5.5: *Predicted versus measured maximum snow height beneath modules. Left: model fitted to all years. Right: model fitted excluding 2022. Points are colored by survey year; the dashed line indicates perfect agreement.*

The spatial distribution of model bias (predicted minus measured) and the corresponding snow height profiles are presented in Figures 5.6 and 5.7, respectively for the model omitting the year 2022.

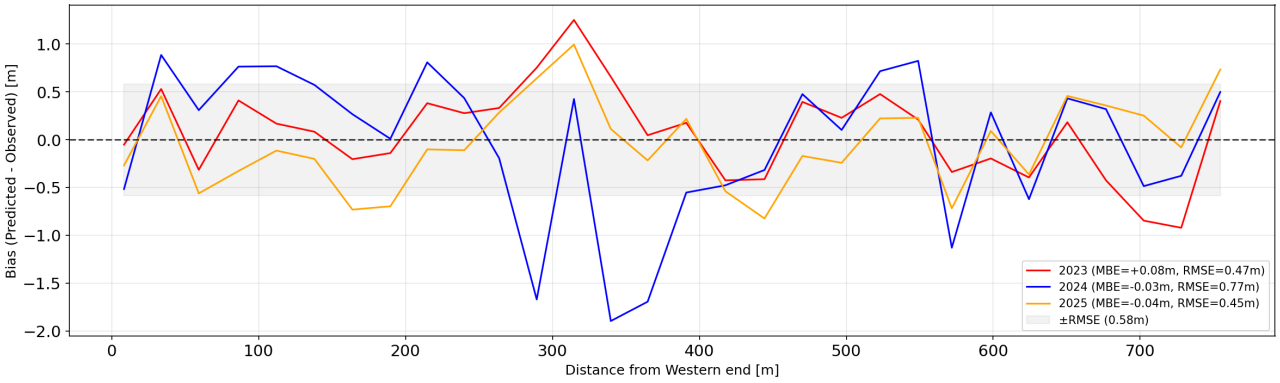


Figure 5.6: *Spatial profile of model bias (predicted − measured) along the dam for each survey year.*

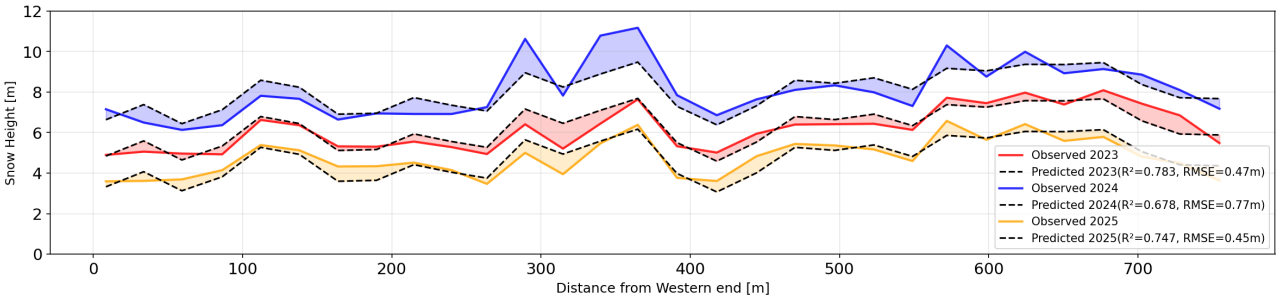


Figure 5.7: *Comparison of measured (solid) and predicted (dashed) snow height profiles along the dam for each survey year.*

The proposed model achieves good accuracy and captures the characteristic spatial variability in snow height along the dam: elevated bimodal accumulation in the curve sector, renewed accumulation toward the eastern end, and a final decline at the dam East extremity.

Wind effects are not explicitly represented by the model parameters, although the dissipation ratio provides an indirect indication of local surface roughness beneath the modules. Preliminary CFD simulations of the wind field during southerly wind events, the most frequent and intense at the site, provide strong evidence that drifting and blowing snow may amplify the accumulation patterns already captured by the geometric parameters. This is particularly apparent in the curve sector, where residual bias is most pronounced, especially during the exceptional 2024 season.

An additional predictor derived from simulated wind fields or a detailed CFD-based snow transport analysis could further improve model performance in areas.

6 Conclusion, Limitations, and Outlook

This report analyzed four years of operational data from the Muttsee power plant, Switzerland's first utility-scale Alpine-PV installation. The key findings can be summarized as follows.

The Alpine-PV concept delivers on its promise at utility scale. Muttsee achieved a mean annual final yield of 1211 kWh/kWp with a winter production share approaching 50%, representing a 14.1% increase over comparable lowland installations and a 1.72-fold improvement in winter share. These results confirm that the advantages observed at test sites translate to commercial-scale deployments.

Under normal snow conditions, snow-induced losses remain modest. Excluding the exceptional 2023/24 season, mean annual losses were 40.7 MWh (2.6% of theoretical production), with interference contributing only 22% of total snow losses.

The sub-module clearance height emerges as a critical design parameter. The 2023/24 winter demonstrated that once snow accumulation beneath modules reaches the panel edge, shedding is impeded, losses escalate dramatically, and structural damage may occur. That season alone accounted for 245.5 MWh of snow-attributable losses (including outage) and required permanent removal of approximately 9% of installed capacity.

An empirical model for predicting maximum snow accumulation beneath modules was developed using drone-based measurements across four winter seasons. The model, based on seasonal maximum snow height, topography-corrected dissipation ratio, and projected panel slant length, achieves $R^2 = 0.89$ and RMSE = 0.58 m when fitted to the 2023–2025 data. Including the 2022 survey reduces performance to $R^2 = 0.59$ and RMSE = 1.23 m. The model captures the characteristic spatial variability along the dam but exhibits residual bias in the curve sector, particularly during 2024, suggesting that wind-transported snow plays a role not yet explicitly parameterized.

Several limitations should be considered when interpreting these results:

Building-integrated versus free-standing configuration. The Muttsee installation is a building-integrated PV (BIPV) system mounted on the dam structure. Current and future Alpine-PV projects will predominantly be free-standing ground-mounted systems with different characteristics. The fixed mounting on the dam constrains module orientations and tilts, resulting in heterogeneous azimuth angles (64% at 198°, 28% at 157°) that differ from optimal configurations. Free-standing systems would allow uniform orientation and potentially higher yields.

Bifaciality effects. The dam-mounted configuration limits rear-side irradiance compared to elevated free-standing structures. Ground-mounted systems with adequate clearance height would benefit more substantially from snow albedo enhancement on the rear side of bifacial modules, potentially increasing winter yields beyond those observed at Muttsee.

Inter-row shading. The single-row configuration along the dam crest eliminates inter-row shading effects that would occur in multi-row free-standing arrays. Operational data from Muttsee therefore cannot directly inform row spacing optimization for ground-mounted Alpine-PV plants.

Site-specific snow dynamics. The dam geometry creates specific wind patterns and snow accumulation characteristics that may not be representative of open-terrain installations. Snow preferential deposition patterns observed at Muttsee are influenced by the dam structure and may differ significantly at free-standing sites.

Several research directions emerge from this work:

Wind-transported snow modeling. The disproportionate snow accumulation observed during the 2023/24 winter and the residual model bias in the curve sector suggest that wind-transported snow (drifting and blowing snow) plays a significant role in interference development, beyond gravitational shedding accumulation. Preliminary CFD simulations of wind fields during southerly events, the most frequent and intense at the site, support this hypothesis. Modeling multi-event, full-season wind-transported snow drift around PV panel arrays represents a critical next step for predicting interference risk and informing clearance height design. Computational fluid dynamics approaches coupled with snow transport models (e.g., snowBedFoam (Hames et al., 2022)) offer promising avenues for this research. An additional predictor derived from simulated wind fields could further improve the empirical model in areas where wind redistribution dominates.

Validation at representative sites. As additional Alpine-PV installations become operational, comparative analysis across sites with varying configurations, elevations, and exposure will enable generalization of findings and refinement of design guidelines for this emerging technology.

References

Abou Yassine, A. H., Namdari, N., Mohammadian, B., and Sojoudi, H. (2022). Understanding mechanisms of snow removal from photovoltaic modules. *Solar Energy*, 231:175–184.

Anderegg, D., Strebel, S., and Rohrer, J. (2023). Alpine Photovoltaik Versuchsanlage Davos Totalp : Erkenntnisse aus 5 Jahren Betrieb. Accepted: 2023-09-29T09:13:16Z.

Andrews, R. W., Pollard, A., and Pearce, J. M. (2013). The effects of snowfall on solar photovoltaic performance. *Solar Energy*, 92:84–97.

Bogenrieder, J., Camus, C., Hüttner, M., Offermann, P., Hauch, J., and Brabec, C. J. (2018). Technology-dependent analysis of the snow melting and sliding behavior on photovoltaic modules. *Journal of Renewable and Sustainable Energy*, 10(2):021005.

Braid, J. L., Riley, D., Pearce, J. M., and Burnham, L. (2020). Image Analysis Method for Quantifying Snow Losses on PV Systems. In *2020 47th IEEE Photovoltaic Specialists Conference (PVSC)*, pages 1510–1516.

Brench, B. (1979). Snow-covering effects on the power output of solar photovoltaic arrays. Technical Report COO–4094-61, 5232456.

Eidevåg, T., Thomson, E. S., Kallin, D., Casselgren, J., and Rasmuson, A. (2022). Angle of repose of snow: An experimental study on cohesive properties. *Cold Regions Science and Technology*, 194:103470.

Haeberlin, H. (2004). Grid Connected PV Plant Jungfraujoch (3454m) in the Swiss Alps: 10 Years of trouble-free Operation with Record Energy Yields.

Hames, O., Jafari, M., Wagner, D. N., Raphael, I., Clemens-Sewall, D., Polashenski, C., Shupe, M. D., Schneebeli, M., and Lehning, M. (2022). Modeling the small-scale deposition of snow onto structured Arctic sea ice during a MOSAiC storm using snowBedFoam 1.0. *Geoscientific Model Development*, 15(16):6429–6449.

Heidari, N., Gwamuri, J., Townsend, T., and Pearce, J. M. (2015). Impact of Snow and Ground Interference on Photovoltaic Electric System Performance. *IEEE Journal of Photovoltaics*, 5(6):1680–1685.

Hostettler, T. (2022). Statistik Sonnenenergie 2022. Technical report, Bundesamt für Energie (BFE), Bern, Switzerland.

Kahl, A., Dujardin, J., and Lehning, M. (2019). The bright side of PV production in snow-covered mountains. *Proceedings of the National Academy of Sciences of the United States of America*.

Lehning, M., Bartelt, P., Brown, B., Fierz, C., and Satyawali, P. (2002). A physical SNOWPACK model for the Swiss avalanche warning Part II. Snow microstructure. *Cold Regions Science and Technology*, 35(3).

Marion, B., Schaefer, R., Caine, H., and Sanchez, G. (2013). Measured and modeled photovoltaic system energy losses from snow for Colorado and Wisconsin locations. *Solar Energy*, 97:112–121.

Pawluk, R. E., Chen, Y., and She, Y. (2019). Photovoltaic electricity generation loss due to snow – A literature review on influence factors, estimation, and mitigation. *Renewable and Sustainable Energy Reviews*, 107:171–182.

Remund, J., Schmutz, M., and Graf (2020). Meteonorm Version 8.

Scherrer, S. C. and Appenzeller, C. (2014). Fog and low stratus over the Swiss Plateau a climatological study. *International Journal of Climatology*, 34(3):678–686.

Townsend, T. and Powers, L. (2011). Photovoltaics and snow: An update from two winters of measurements in the SIERRA. pages 003231–003236.

von Rütte, F., Kahl, A., Rohrer, J., and Lehning, M. (2021). How Forward-Scattering Snow and Terrain Change the Alpine Radiation Balance With Application to Solar Panels. *Journal of Geophysical Research: Atmospheres*, 126(15).

A Technical Specifications

This appendix provides detailed technical specifications for all components of the Muttsee PV power plant, complementing the overview presented in Section 2. Data sheets and specifications of data Loggers, irradiance and temperature sensors, transformers, inverters, combining string-boxes and PV modules can be obtained upon request.

String Specifications

Table A.1 provides the complete specifications for each of the 23 strings, including orientation, module composition, and nominal power.

String	Azimuth [°]	Tilt [°]	Type 1 (485 Wp)	Type 2 (385 Wp)	Total Modules	Capacity [kWp]
1	157	65	162	51	213	94.155
2	157	65	198	33	231	103.785
3	157	51	198	33	231	103.785
4	157	51–65	180	30	210	94.350
5	157	65	198	33	231	103.785
6	157	65	198	33	231	103.785
7	≤175.2	65	150	60	210	92.100
8	<198	51–65	150	60	210	92.100
9	198	65	162	27	189	84.915
10	198	51	180	30	210	94.350
11	198	51	180	30	210	94.350
12	198	65	162	27	189	84.915
13	198	51	198	33	231	103.785
14	198	65	162	27	189	84.915
15	198	51	180	30	210	94.350
16	198	51	198	33	231	103.785
17	198	51	180	30	210	94.350
18	198	65	162	27	189	84.915
19	198	51	180	30	210	94.350
20	198	51	180	30	210	94.350
21	198	51	180	30	210	94.350
22	198	51	180	30	210	94.350
23	198	51	180	30	210	94.350
Total	–	–	**4098**	**777**	**4875**	**2184.225**

Table A.1: *Detailed specifications for each string in their original state. Strings 4, 7, and 8 span multiple tilt or azimuth values due to their position on the dam. Strings 7 and 8 are located in the curve sector, resulting in variable azimuths. All azimuths are measured clockwise from North.*

Tilt–Azimuth Distribution

Table A.2 presents the rated power distribution across all tilt and azimuth combinations, accounting for the variability within strings 4, 7, and 8.

	157°	161.6°	166.1°	170.7°	175.2°	179.8°	184.3°	188.9°	193.4°	198°	Sum
51°	0.06	–	–	–	–	–	–	–	0.01	0.48	0.56
65°	0.22	0.01	0.01	0.01	0.01	0.01	0.01	0.01	0.01	0.16	0.44
Sum	0.28	0.01	0.01	0.01	0.01	0.01	0.01	0.01	0.02	0.64	1.00

Table A.2: *Rated power ratio (kWp/kWp$_{total}$) for each tilt–azimuth combination. Dashes indicate non-existent combinations. The majority of installed capacity (64%) is oriented at 198° azimuth, with 28% at 157°. The tilt distribution is 56% at 51° and 44% at 65°.*

PV Modules

Two bifacial module types from Megasol are installed at the plant, as detailed in Table A.3.

Type	Manufacturer	Model	Nominal Power [Wp]
1	Megasol	M460-HC144-w BF GG U40	485
2	Megasol	M385-HC120-w BF GG U40	385

Table A.3: *PV module specifications. Both types are bifacial glass-glass modules.*

Electrical layout

Figure A.1 details the electrical layout of the plant.

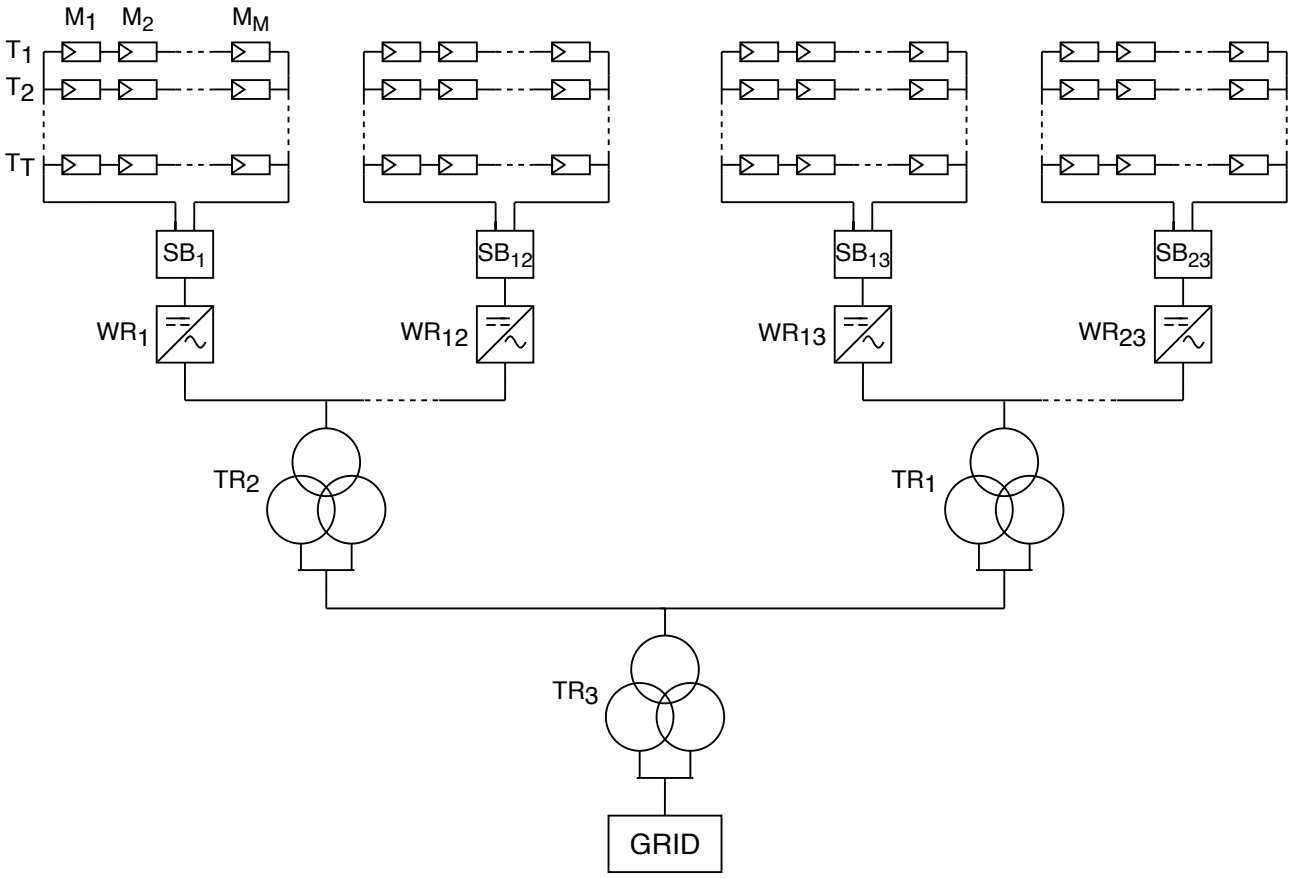


Figure A.1: *Plant electrical layout. The number of modules per table varies between 189 and 231, and the number of tables per string ranges from 9 to 11, resulting in string capacities between 85 kWp and 104 kWp. Strings 1–12 connect to transformer TR2, while strings 13–23 connect to TR1. A third transformer (TR3) in Tierfehd connects the plant to the 50 kV grid.*

Combining String-Boxes

Each table within a string is connected in parallel to a combining string-box. The string-boxes are equipped with:

- **DC-DC converter:** Mornsun PV 15-29B24A10, which adjusts voltage to match the maximum power point tracker (MPPT) commands from the connected inverter.
- **Controller:** Kernel Sistemi ST2N 1240, a 12-channel combining board equipped with a performance monitoring unit (PMU) that provides table-level power measurements.

Inverters

Power conditioning is performed by 23 identical inverters with the specifications listed in Table A.4.

Parameter	Value
Model	KACO blueplanet 105 TL3
Max. DC input power	157.5 kW
Max. DC input voltage	1450 V
Max. DC input current	183 A
AC output	3-phase, 400 V, 50 Hz
Max. AC output power	105 kW
Efficiency	98.9%

Table A.4: *Inverter specifications.*

Each inverter is equipped with a PMU providing string-level power measurements.

Transformers

Two transformers (TR1 and TR2) manufactured by Rauscher & Stoecklin are located in the dam's access building alongside the inverters. Their specifications are given in Table A.5.

Parameter	Value
Manufacturer	Rauscher & Stoecklin
AC input voltage	400 V
AC output voltage	16 kV
Nominal power	1.25 MW
Efficiency	99.3%

Table A.5: *On-site transformer specifications. Strings 1–12 connect to TR2; strings 13–23 connect to TR1.*

A third transformer (TR3), located in Tierfehd in the valley, steps up the voltage from 16 kV to 50 kV for grid injection.

Irradiance and Temperature Sensors

Combined irradiance–temperature sensors (meteocontrol SI-RS485TC-T-Tm-MB) are installed in the plane of array for each of the four main tilt–azimuth configurations. Each configuration is monitored by two sensors: one at the table edge measuring front-side POA irradiance, and one at the center measuring rear-side (backsheet) POA irradiance. Table A.6 lists the sensor positions.

Sensor	Block	String	Table	Azimuth [°]	Tilt [°]
Blck34, 65°, E+T, in/out	34	4	8	157	65
Blck34, 51°, E+T, in/out	34	4	9	157	51
Blck25, 65°, E+T, in/out	25	12	9	198	65
Blck25, 51°, E+T, in/out	25	13	7	198	51

Table A.6: *Position and orientation of the combined irradiance–temperature sensors. Sensors on block 34 cover the 157° azimuth configurations; sensors on block 25 cover the 198° configurations.*

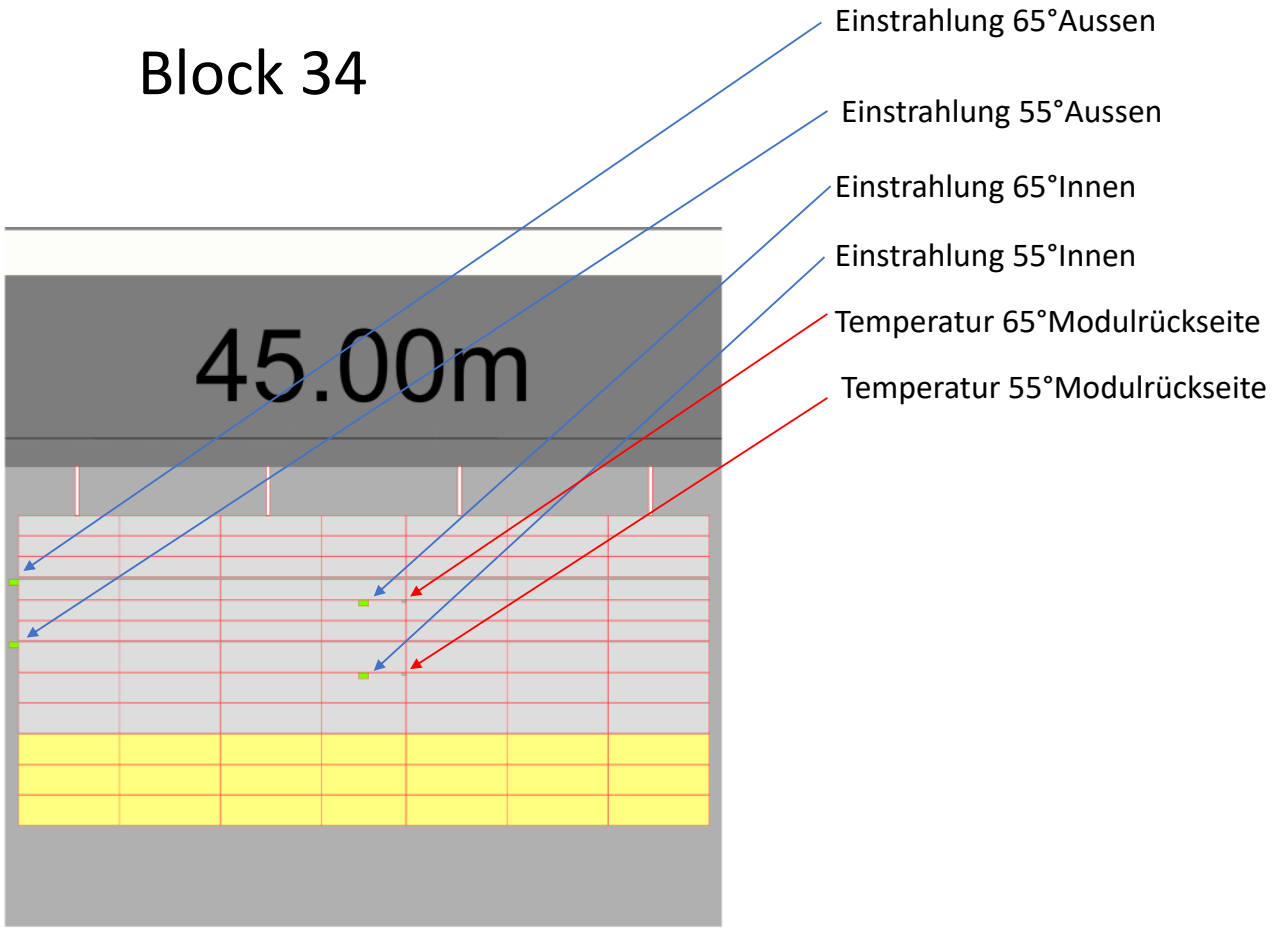


Figure A.2: *Location of irradiance and temperature sensors on block 34 (West side), covering tilt–azimuth combinations of 51° and 65° at 157° azimuth.*

Data Loggers

Two data loggers (meteocontrol XC-3000 and XM-200) record the PMU outputs from both the inverters and the combining string-boxes at 1-minute resolution. Data is transmitted directly to the meteocontrol VCOM cloud platform for storage and retrieval.

B Drone Surveys

Annual drone surveys were conducted using a Wingtra One (first generation) equipped with a Sony DSC-RX1RM2 camera (35 mm focal length) and a post-processed kinematic (PPK) GNSS receiver. Georeferencing was performed using a virtual reference station from the AGNES network operated by swisstopo. Photogrammetric processing was carried out in Agisoft Metashape Pro to generate orthomosaics and digital elevation models (DEMs). Snow height maps were computed by differencing winter and summer DEMs. Ground control points distributed along the power plant served as independent check points for accuracy assessment. Table B.1 reports the root mean square error (RMSE) for each survey.

RMSE [cm]	Ground	2022	2023	2024	2025
Z	4.4	3.7	44.7	0.6	10.9
X	2.5	1.7	12.9	6.1	12.5
Y	2.8	1.7	60.6	11.7	15.2
Total	5.7	4.4	62.0	13.2	22.5

Table B.1: *Root mean square error of drone survey georeferencing by axis and year.*

C Plant Outage 2024: Detailed Table-Level Evolution Maps

This appendix provides detailed spatial views of the capacity evolution during the 2024 outage phases described in Section 4. Figure C.1 shows the operational status of individual module tables across the four outage phases (L1–L4), while Figure C.2 summarizes the corresponding string-level capacity over time.

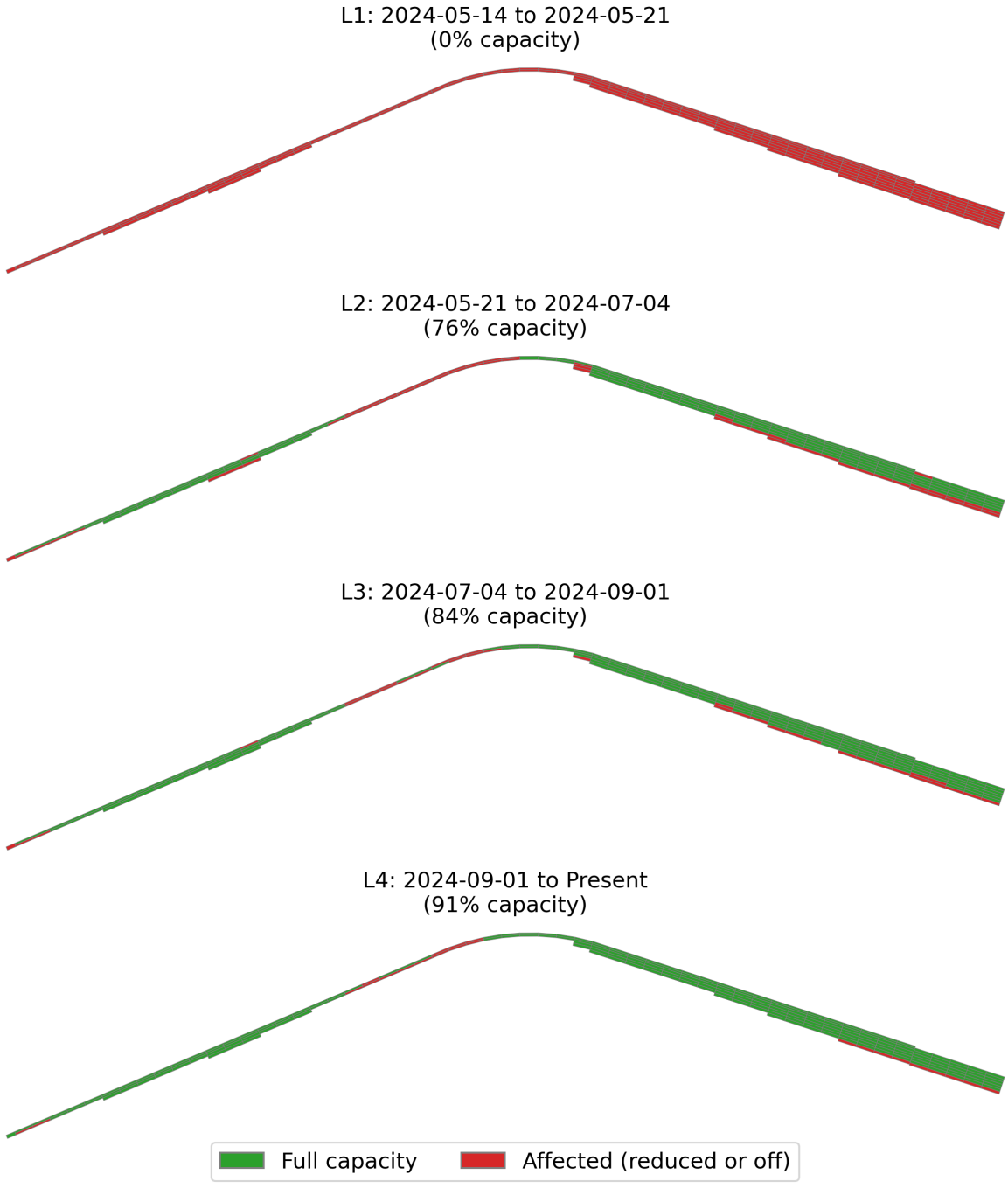


Figure C.1: *Table-resolved plan view of the evolution of the capacity during the outage phases in 2024.*

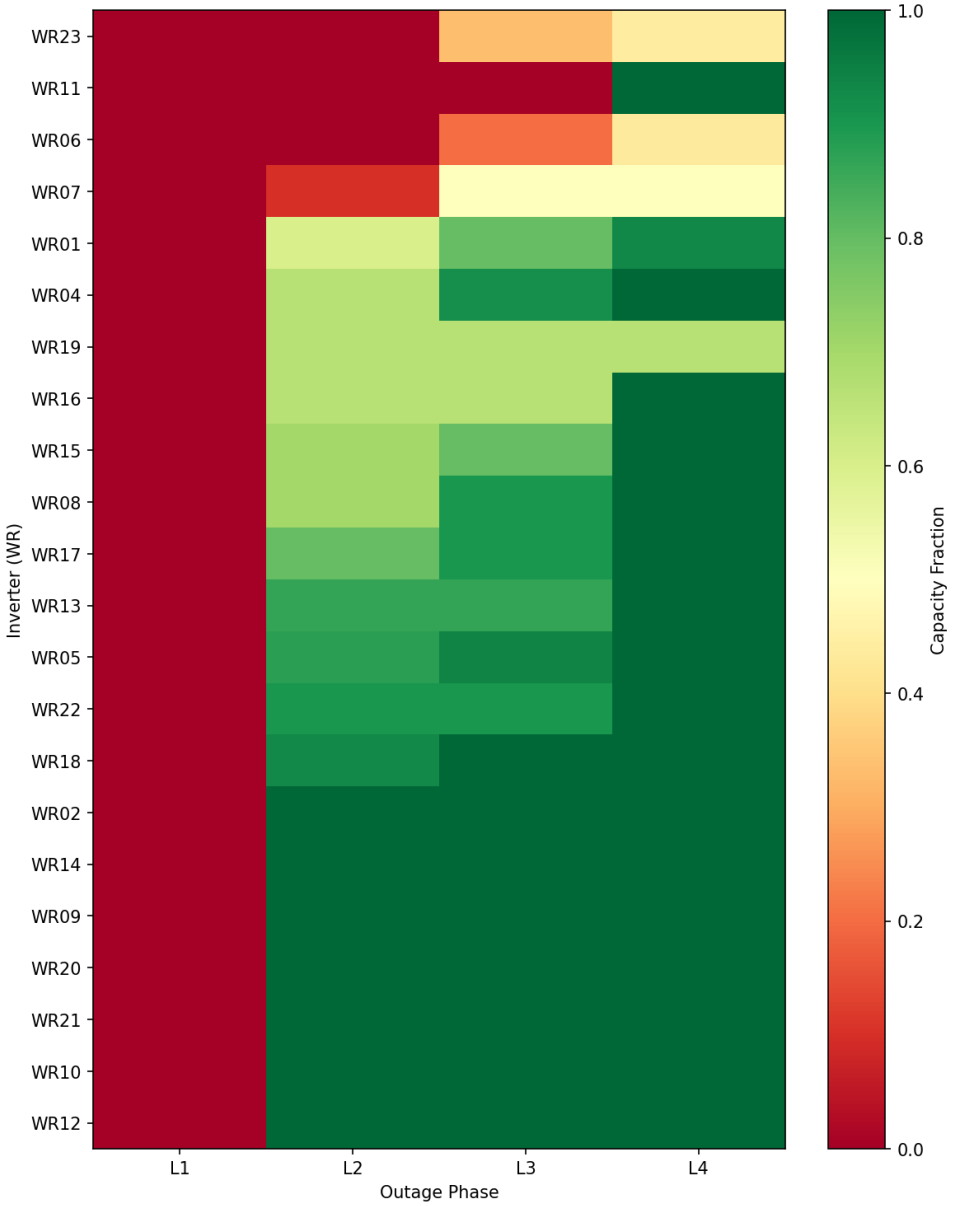


Figure C.2: *String-level capacity evolution during the 2024 outage phases. Each row represents one inverter string (WR); color intensity indicates operational capacity.*

D Snow Event Catalogue

This appendix provides the complete catalogue of snow events recorded at the Muttsee power plant across the three monitored winter seasons. Events were identified through visual inspection of the camera system imagery (Section 4).

Abbreviation	Description
light / moderate / heavy / extreme	Snow accumulation intensity
multi-day	Event spanning multiple days
solar melt W→E	Cleared by solar irradiance, west to east progression
low-irrad. clearing	Cleared under low irradiance conditions
wind-assisted	Wind contributed to snow removal
rime-like	Accumulation resembling rime ice
persistent 50°	Snow remained longer on 50° panels
persistent patches	Residual snow patches after main clearing
stormy	Stormy conditions during event
gaps	Missing camera images
low visibility	Poor visibility due to weather/optics
Interference flags: C = Curve sector, E = East sector, W = West sector	

Table D.1: *Legend for snow event descriptions and interference flags.*

#	Start	End	Interf.	Description
1	04.11.22 05:15	06.11.22 12:05	–	multi-day
2	09.11.22 18:30	10.11.22 09:25	–	–
3	16.11.22 05:30	16.11.22 11:00	–	–
4	18.11.22 11:30	19.11.22 13:05	–	solar melt W→E, stormy
5	20.11.22 06:00	20.11.22 12:10	–	persistent 50°
6	22.11.22 06:00	23.11.22 09:00	–	–
7	26.11.22 05:45	26.11.22 11:05	–	solar melt W→E
8	29.11.22 06:00	01.12.22 11:25	–	multi-day, stormy
9	04.12.22 07:45	06.12.22 11:00	–	multi-day, solar melt W→E
10	10.12.22 07:20	12.12.22 12:15	–	multi-day
11	13.12.22 10:20	14.12.22 10:50	–	light
12	16.12.22 07:05	17.12.22 10:40	–	solar melt W→E
13	21.12.22 06:30	21.12.22 13:00	–	light, low-irrad. clearing
14	23.12.22 07:10	26.12.22 11:50	–	gaps
15	30.12.22 06:30	30.12.22 09:25	–	light, solar melt W→E
16	30.12.22 14:45	31.12.22 08:00	–	light, low-irrad. clearing
17	03.01.23 07:00	03.01.23 11:00	–	low-irrad. clearing
18	04.01.23 06:30	04.01.23 09:10	–	light, solar melt W→E
19	05.01.23 13:10	05.01.23 16:10	–	light, low-irrad. clearing
20	09.01.23 06:30	14.01.23 14:45	–	multi-day, stormy
21	15.01.23 13:35	16.01.23 15:35	–	persistent 50°
22	18.01.23 06:30	18.01.23 12:00	–	light, solar melt W→E, gaps
23	18.01.23 15:55	23.01.23 12:10	–	low-irrad. clearing
24	31.01.23 06:15	31.01.23 11:55	–	light, solar melt W→E
25	02.02.23 06:25	03.02.23 10:45	–	light, solar melt W→E, gaps
26	05.02.23 13:25	06.02.23 11:45	–	solar melt W→E, gaps
27	23.02.23 05:30	23.02.23 09:00	–	light, solar melt W→E
28	26.02.23 05:45	27.02.23 11:30	–	multi-day, solar melt W→E, stormy
29	09.03.23 05:15	09.03.23 08:05	–	light
30	10.03.23 11:20	11.03.23 10:10	–	light, low-irrad. clearing
31	14.03.23 08:00	16.03.23 15:10	C	multi-day, solar melt W→E, persistent patches, gaps
32	24.03.23 13:45	30.03.23 09:55	C	multi-day, stormy
33	31.03.23 08:20	04.04.23 08:20	C	multi-day, stormy
34	07.04.23 04:30	07.04.23 16:25	C	light, gaps
35	09.04.23 06:55	09.04.23 11:40	C	light, solar melt W→E, gaps
36	11.04.23 04:25	12.04.23 10:05	C	low-irrad. clearing
37	12.04.23 17:15	17.04.23 15:05	C/E/W	multi-day, stormy

Table D.2: *Snow events during winter W22/23. Timestamps in dd.mm.yy HH:MM format.*

#	Start	End	Interf.	Description
38	15.10.23 05:00	16.10.23 08:00	–	light, solar melt W→E
39	21.10.23 12:35	22.10.23 12:20	–	moderate, solar melt W→E, gaps
40	24.10.23 15:00	25.10.23 10:05	–	light, solar melt W→E
41	27.10.23 05:15	27.10.23 12:00	–	moderate, solar melt W→E
42	28.10.23 05:30	28.10.23 09:00	–	light, solar melt W→E, gaps
43	31.10.23 05:30	06.11.23 11:35	–	multi-day, stormy
44	08.11.23 05:45	08.11.23 08:55	–	light, solar melt W→E
45	10.11.23 06:45	13.11.23 12:20	–	light, multi-day, solar melt W→E
46	14.11.23 08:30	14.11.23 11:10	–	light, solar melt W→E, low visibility
47	15.11.23 09:45	16.11.23 12:40	–	moderate, low visibility
48	18.11.23 06:00	19.11.23 06:00	–	gaps
49	19.11.23 08:15	19.11.23 11:20	–	light
50	21.11.23 06:00	22.11.23 12:45	–	moderate
51	26.11.23 09:10	17.12.23 13:40	C/E/W	extreme, low visibility
52	01.01.24 06:30	02.01.24 10:55	C/E	light
53	03.01.24 06:30	03.01.24 11:10	C/E	light
54	05.01.24 14:25	11.01.24 09:55	C/E/W	multi-day
55	17.01.24 06:30	17.01.24 10:45	C/E/W	light, solar melt W→E
56	19.01.24 06:30	20.01.24 15:35	C/E/W	moderate, solar melt W→E
57	25.01.24 06:15	28.01.24 12:45	C/E/W	multi-day
58	01.02.24 11:50	03.02.24 11:10	C/E/W	light, multi-day
59	11.02.24 06:15	12.02.24 11:30	C/E/W	light, solar melt W→E
60	13.02.24 06:00	13.02.24 12:35	C/E/W	light
61	19.02.24 06:00	21.02.24 11:50	C/E/W	multi-day
62	23.02.24 05:45	27.02.24 13:30	C/E/W	multi-day
63	01.03.24 05:30	04.03.24 09:30	C/E/W	multi-day, solar melt W→E
64	05.03.24 08:40	07.03.24 12:45	C/E/W	multi-day
65	11.03.24 05:15	11.03.24 12:40	C/E/W	light
66	12.03.24 05:15	12.03.24 14:35	C/E/W	light
67	14.03.24 07:10	15.03.24 15:00	C/E/W	moderate, gaps
68	21.03.24 13:30	22.03.24 10:40	C/E/W	light, gaps
69	23.03.24 08:50	25.03.24 13:05	C/E/W	multi-day, solar melt W→E
70	27.03.24 10:45	28.03.24 13:30	C/E/W	light, low-irrad. clearing
71	28.03.24 14:40	29.03.24 04:45	C/E/W	light, low-irrad. clearing
72	01.04.24 05:10	02.04.24 12:05	C/E/W	moderate, solar melt W→E, persistent 50°
73	09.04.24 15:10	11.04.24 09:15	C/E/W	moderate, solar melt W→E, persistent 50°
74	16.04.24 04:00	16.04.24 09:20	C/E/W	light, low-irrad. clearing, persistent 50°
75	17.04.24 04:00	22.04.24 12:00	C/E/W	heavy, multi-day

Table D.3: *Snow events during winter W23/24. Timestamps in dd.mm.yy HH:MM format.*

#	Start	End	Interf.	Description
76	12.11.24 05:45	13.11.24 11:45	–	light, solar melt W→E
77	19.11.24 07:10	19.11.24 12:15	–	light
78	20.11.24 10:00	24.11.24 11:15	–	moderate, multi-day, solar melt W→E, persistent 50°
79	26.11.24 06:00	26.11.24 09:45	–	light, solar melt W→E
80	28.11.24 06:15	29.11.24 13:30	–	moderate, solar melt W→E, persistent 50°
81	02.12.24 06:15	02.12.24 09:15	–	light, solar melt W→E
82	03.12.24 06:15	05.12.24 13:20	–	moderate, multi-day, solar melt W→E, persistent 50°
83	07.12.24 14:50	10.12.24 12:25	–	moderate, multi-day, solar melt W→E, persistent 50°
84	14.12.24 12:25	16.12.24 10:40	–	light, solar melt W→E
85	20.12.24 15:10	25.12.24 13:30	–	heavy, multi-day
86	03.01.25 06:30	04.01.25 12:40	–	moderate, solar melt W→E
87	05.01.25 06:30	05.01.25 10:15	–	light, wind-assisted
88	07.01.25 06:30	07.01.25 11:30	–	light, solar melt W→E
89	08.01.25 06:30	08.01.25 13:00	–	light, low-irrad. clearing
90	09.01.25 15:40	13.01.25 14:20	–	moderate, multi-day, persistent 50°
91	15.01.25 10:00	15.01.25 12:50	–	light, low-irrad. clearing
92	20.01.25 06:15	20.01.25 09:35	–	light
93	23.01.25 08:45	23.01.25 12:55	–	light
94	26.01.25 06:15	26.01.25 11:45	–	moderate, solar melt W→E, persistent 50°
95	28.01.25 08:30	29.01.25 13:30	C	moderate, solar melt W→E, persistent 50°
96	12.02.25 06:00	12.02.25 13:15	C	light
97	13.02.25 06:15	13.02.25 09:10	C	light, rime-like
98	14.02.25 06:00	15.02.25 13:05	C	moderate, solar melt W→E
99	25.02.25 05:30	24.02.25 09:20	C	light, rime-like, gaps
100	25.02.25 16:10	27.02.25 09:15	C	light, solar melt W→E, persistent patches
101	27.02.25 14:05	28.02.25 12:55	C	light
102	01.03.25 05:30	01.03.25 09:05	C	light, solar melt W→E
103	11.03.25 05:15	11.03.25 08:20	C	light, solar melt W→E
104	13.03.25 06:05	14.03.25 13:40	C	moderate, multi-day, solar melt W→E
105	15.03.25 05:00	15.03.25 08:35	C	light
106	16.03.25 05:30	17.03.25 12:45	C	light, low-irrad. clearing

Table D.4: *Snow events during winter W24/25. Timestamps in dd.mm.yy HH:MM format.*

E Principal Component Analysis

This appendix provides supplementary details on the principal component analysis performed to inform predictor selection for the interference height model (Section 5).

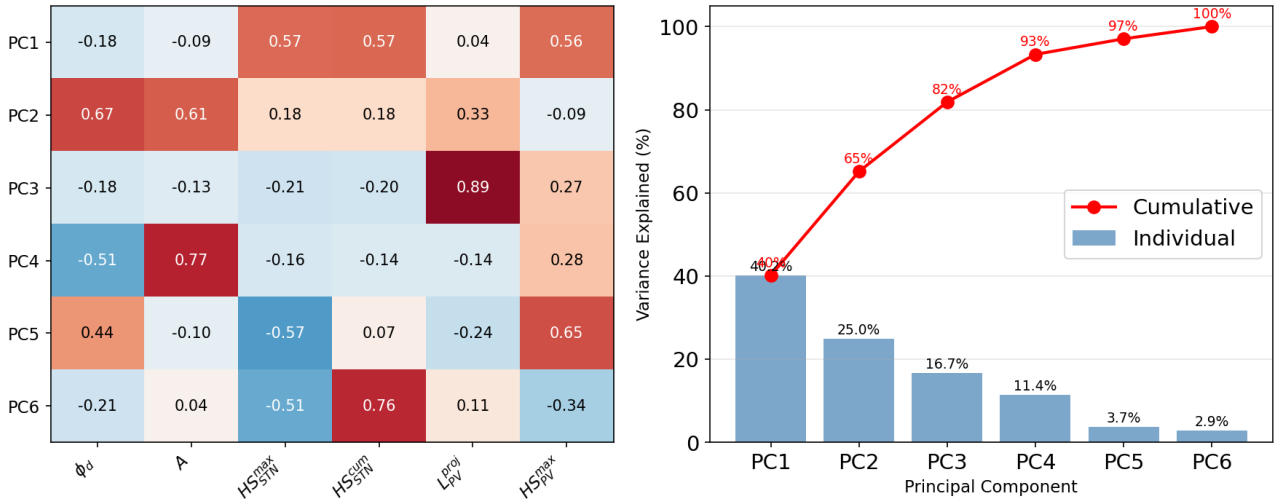


Figure E.1: *PCA loadings and explained variance. Left: correlation coefficients between principal components and original variables. Right: scree plot showing variance explained by each component (cumulative variance in parentheses).*

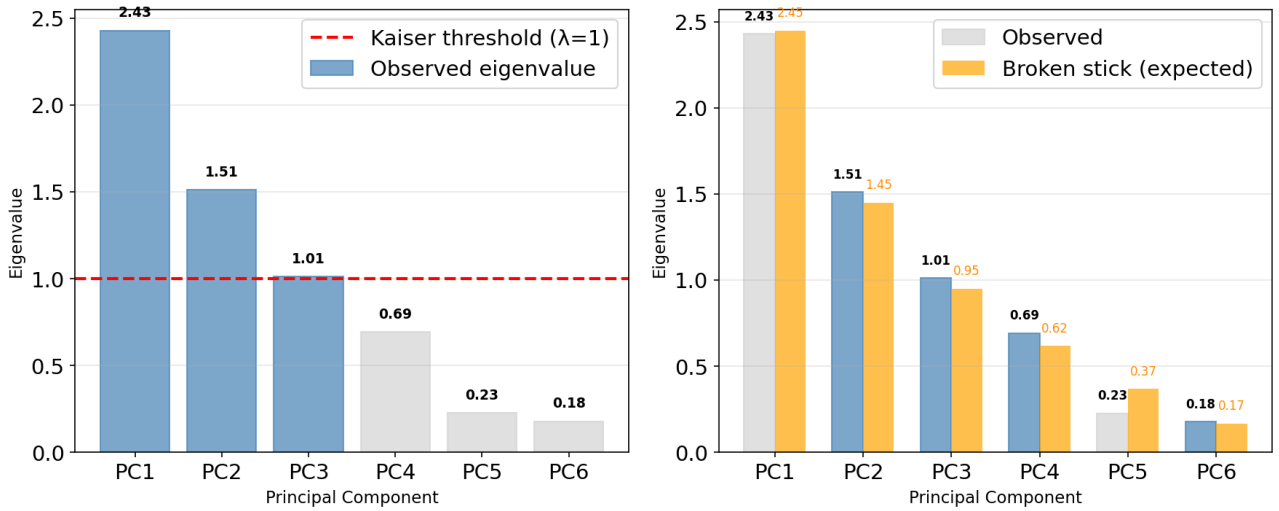


Figure E.2: *Component selection criteria. The Kaiser criterion (eigenvalue > 1) suggests retaining three components. The broken stick method suggests four components, excluding PC1.*